

Relationships between Immersion Freezing and Crystal Habit for Arctic Mixed-Phase Clouds—A Numerical Study

TEMPEI HASHINO

School of Environmental Science and Engineering, Kochi University of Technology, Kami, Japan

GIJS DE BOER

Cooperative Institute for Research in Environmental Sciences, University of Colorado Boulder, Boulder, Colorado

HAJIME OKAMOTO

Research Institute for Applied Mechanics, Kyushu University, Fukuoka, Japan

GREGORY J. TRIPOLI

Atmospheric and Oceanic Sciences, University of Wisconsin–Madison, Madison, Wisconsin

(Manuscript received 11 March 2020, in final form 2 May 2020)


ABSTRACT

The number concentration of ice particles in Arctic mixed-phase clouds is a major controlling factor of cloud lifetime. The relationships between ice nucleation mode and ice crystal habit development are not yet constrained by observations. This study uses a habit-predicting microphysical scheme within a 3D large-eddy simulation model to evaluate the relationship between immersion freezing and ice habit in a simulated Arctic mixed-phase cloud case. Three immersion freezing parameterizations are considered: a volume-dependent freezing scheme (VF), a parameterization limited to activated droplets (C-AC), and a parameterization limited to coarse aerosol particles (C-CM). Both C-AC and C-CM are based on classical nucleation theory. The freezing rate with VF is found to be greater in downdraft regions than in updraft regions due to the downdraft having a higher number concentration of large droplets. The C-AC cases show active freezing of small droplets near cloud top, whereas in the C-CM cases, mainly the 8–32- μm -sized droplets freeze in updraft regions near the cloud base. Because the initial crystal size is assumed to affect the axis ratio of hexagonal plates, the VF cases produce crystals with larger axis ratios, resulting in smaller mode radii than the C-AC cases. In all cases, irregular polycrystals dominate near cloud top and a band-like structure develops within the cloud, which qualitatively agrees with previous observations. In the VF and C-CM cases, unactivated large droplets arising from coarse-mode aerosol particles contributed significantly to the freezing rate, producing an important influence on crystal habit.

1. Introduction

The Arctic has been warming more than the rest of the world under the increasing greenhouse gas concentrations (e.g., Manabe and Wetherald 1975; Hansen et al. 2005). Here, recent rises in near-surface and lower-troposphere temperatures during winter have been attributed in part to an increasing loss of the sea ice cover, allowing for

increased heat transfer from the ocean (Serreze et al. 2009). In an atmosphere–ocean system at equilibrium, radiative effects of water vapor and clouds and large-scale condensation are the most important warming factors, next to ocean heat release during winter (Yoshimori et al. 2017). Due to the demonstrated extended persistence of supercooled liquid droplets (e.g., Morrison et al. 2012), and the overall warming of the surface by longwave emission from high-latitude stratiform clouds (e.g., Shupe and Intrieri 2004; Hashino et al. 2016), an increase in cloud cover can act as a positive feedback to any warming of the climate system. Therefore, the microphysics and radiative effects of mixed-phase clouds have to be properly understood.

 Denotes content that is immediately available upon publication as open access.

Corresponding author: Tempei Hashino, hashino.tempei@kochi-tech.ac.jp

DOI: 10.1175/JAS-D-20-0078.1

© 2020 American Meteorological Society. For information regarding reuse of this content and general copyright information, consult the [AMS Copyright Policy](#) (www.ametsoc.org/PUBSReuseLicenses).

The ice crystals coexisting with liquid droplets in mixed-phase clouds can grow at the expense of the liquid because the saturation vapor pressure over ice is lower than that over liquid [known as the Wegener–Bergeron–Findeisen (WBF) process; Wegener 1911; Bergeron 1935; Findeisen 1938]. To maintain liquid droplets in a rising air parcel, a certain amount of upward air motion is necessary to help produce sufficient regions of supersaturation through adiabatic cooling to overcome vapor consumption by ice crystals. Condensation on liquid droplets therefore depends in part on the ice number concentration (e.g., Pinsky et al. 2015) and thereby the ice nucleation (IN) process. However, both the dominant ice nucleation modes and the chemical and physical characteristics of ice nucleating particles (INPs) relevant for mixed-phase stratiform clouds are under debate (e.g., Rangno and Hobbs 2001; Fridlind et al. 2007; Paukert and Hoose 2014). Analyses completed using surface-based remote sensors at several Arctic sites (de Boer et al. 2011) suggest that most mixed-phase clouds are initiated with liquid droplets forming from haze particles, then ice forms and precipitates, and the ice precipitation stops when the liquid droplets disappear. This implies a likely role for liquid-dependent nucleation processes (e.g., immersion freezing, contact freezing), though it does not necessarily rule out deposition nucleation of ice crystals. Further supporting the role of liquid-dependent ice nucleation, a numerical study by Young et al. (2017) showed that when ice nucleation parameterizations were allowed to act only under water-saturated conditions, cloud microphysical quantities were comparable to aircraft observations.

In addition to the central role of ice nucleation, ice particle growth processes through vapor deposition, riming, and aggregation play important roles in governing cloud lifetime (e.g., Borys et al. 2003; Liu et al. 2003; Mitchell et al. 2006; Harrington et al. 2009; Hashino and Tripoli 2011b; Lance et al. 2011). In addition, the period of time during which an individual crystal can remove vapor from the mixed-phase layer depends on the crystal shape and density. For example, Avramov and Harrington (2010) showed that the ice crystal habit assumed in cloud-resolving simulations can modulate the sensitivity of liquid and ice-water path to ice-number concentration through vapor-depositional growth and fall speed. Furthermore, parcel-model simulations by Sulia and Harrington (2011) indicate that predicting the axis ratio (same as axial and aspect ratio) of spheroidal ice particles affects cloud glaciation time, especially with ice number concentrations from 1 to 100 L⁻¹ and temperatures from -6 to -15°C. Despite observational studies of the axis ratio of ice crystals and particle types in mixed-phase clouds (e.g., Matrosov et al. 2017;

Wen et al. 2016), relationships between ice crystal habit, environmental conditions, vertical velocity, and aerosol amounts are still largely unconstrained.

Given that the extent of ice crystal vapor deposition, riming, and aggregation within a cloud are influenced by the number of ice particles as well as the shape and density of crystals, the mode of ice nucleation may influence the resulting ice particle population. Laboratory experiments show that both the crystal habit and ice nucleation modes depend on the environmental temperature and supersaturation (e.g., Bailey and Hallet 2009; Hoose and Mohler 2012). In the present study, we use three-dimensional (3D) large-eddy simulations (LESs) of a mixed-phase cloud to 1) identify possible relations between ice crystal habits and the ice nucleation process, and 2) compare the impact of using a volume-dependent freezing parameterization in contrast to using classical nucleation theory (CNT)-based schemes. Investigation of the first goal has not previously been undertaken and is only possible due to the recent advancement of microphysical schemes to simulate changing ice crystal aspect ratios in a cloud model (e.g., Hashino and Tripoli 2007; Harrington et al. 2013; Chen and Tsai 2016; Jensen et al. 2017). The second goal is motivated by previous results that indicate a potentially dominant role of the immersion freezing process in the maintenance of mixed-phase clouds (de Boer et al. 2010, 2013). For example, de Boer et al. (2010) argued that the rapid gravitational removal of large ice crystals formed by freezing relatively large droplets and the survival of small haze droplets (due to their lower freezing points) helped to maintain mixed-phase cloud conditions. However, the hypothesis was developed using a common empirical parameterization of immersion freezing (Bigg 1953; Diehl and Wurzler 2004) and did not consider freezing of haze particles or deliquescence heterogeneous freezing. This motivates us to extend our previous work through the implementation of a CNT based parameterization within a habit-predicting microphysical scheme [Advanced Microphysics Prediction System (AMPS); Hashino and Tripoli 2007], and evaluate the sensitivity of these previous results to the nucleation scheme.

In section 2, we briefly describe the dynamical model and AMPS, then explain the three immersion freezing parameterizations, the numerical experiments, and a radar simulator that accounts for ice crystal shapes. In section 3, we discuss the 3D structure of simulated habits, and the relationships among cloud droplet characteristics, ice particle size distributions, axis ratios of hexagonal plates, and links to droplet freezing schemes. The simulations are constrained to maintain the liquid-water path and have a realistic simulation of

TABLE 1. Prognostic particle property variables defined for each mass bin in SHIPS and SLIPS and for each category in APS. New variables added for this study are indicated by boldface font. PPVs are predicted together with number concentration and mass content of each bin or category.

SHIPS: Subdistributions with piecewise linear or cubic polynomial	
Mass content components	Ice crystal mass, rime mass, aggregation mass, meltwater mass, frozen-nucleation mass
Length variable components	<i>a</i> -axis length, <i>c</i> -axis length, dendrite branch length, coordinates of center of gravity of a polycrystal
Concentration component	Number of extra crystalline structures, number of activated INP, number of INP
Volume variable components	Circumscribing sphere volume
Aerosol mass content components	Aerosol total mass, aerosol soluble mass
SLIPS: Subdistributions with piecewise linear or cubic polynomial	
Concentration component	Number of activated INP, number of INP
Aerosol mass content components	Aerosol total mass, aerosol soluble mass
APS: Lognormal particle size distributions	
Concentration component	Number of activated INP, number of INP
Mass content components	Soluble mass

radar reflectivity. In [section 4](#), we discuss the importance of predicting a mass–dimensional relationship and large unactivated droplets.

2. Methodology

a. Atmospheric model

The 3D LES model used for the experiments is the University of Wisconsin nonhydrostatic modeling system (UW-NMS; [Tripoli and Smith 2014a,b](#)). The momentum equation is cast into enstrophy-conserving form with a variable-stepped topographic lower boundary condition. The turbulence diffusion is solved with a 1.5-order turbulent kinetic energy (TKE) predicting closure, while a Monin–Obukhov similarity scheme is applied for the surface layer. Conservative scalars include ice–liquid water potential temperature θ_{il} , specific mass of total water, and specific quantities relevant to aerosol particles and hydrometeors. The shortwave and longwave broadband fluxes are calculated with the Rapid Radiative Transfer Model for GCMs (RRTMG; [Iacono et al. 2008](#)), which uses a correlated-*k* approach and two-stream approximation. To keep the relationships among the specific quantities within a realistic range, especially for simulation of well-mixed boundary layer clouds, we did not apply numerical filtering and turbulence mixing to hydrometeor-specific quantities such as mass content, number concentration, and the particle property variables that are introduced below.

b. Cloud microphysics model

The AMPS consists of aerosol, liquid, and ice modules ([Hashino and Tripoli 2007, 2008, 2011a,b](#)). The ice module, the Spectral Ice Habit Prediction System (SHIPS), uses a continuous-property approach to simulating ice particle

properties in a mass-bin-defined spectrum. Currently, SHIPS predicts 16 particle property variables (PPVs) in addition to number concentration and mass content for each mass bin ([Table 1](#)). The PPVs are integrated in time and space based on cloud microphysical processes occurring in the grid volumes. To study ice nucleation processes, we added three variables: frozen nucleation mass, the number of INPs, and the number of activated INPs. The frozen nucleation mass records the initial size of the frozen droplets. We also use this quantity to help determine the spatial distribution of quasi-spherical particles, a common type of particle in Arctic clouds (details in [appendix A](#)). The number concentrations of INPs and activated INPs are used to diagnose the minimum contact angle of ice over a substrate (details in the next section). The liquid mass spectrum is simulated with four PPVs in each bin, whereas the size spectra of aerosol particles is simulated with three PPVs ([Table 1](#)). This version applies a cubic polynomial function to represent the subdistribution in a bin ([Dinh and Durran 2012](#)), which improves the transfer processes between bins.

The wet transfer scheme in which dry aerosol particles in the aerosol categories enter the liquid mass spectrum is relevant to the immersion freezing process. In AMPS, supersaturation with respect to water at the end of a sub-time step is iteratively solved under the constraints of conservation of moist entropy and total water, similar to that in [Walko et al. \(2000\)](#). We use a 10-bin particle size distribution for aerosol, with the critical supersaturation for each bin calculated separately. During an iteration, any bin with a critical supersaturation below the environmental supersaturation is marked for transfer into the liquid spectrum. The fraction of marked particles that

are transferred is set to be the ratio of the obtained supersaturation to the maximum supersaturation necessary to “wet” the aerosol particles. We assume that this “wet” state occurs when the water mass reaches 5% of the aerosol mass. (The 5% value is somewhat arbitrary, but we found our results insensitive to the value.) In contrast, [de Boer et al. \(2013\)](#) used the critical radius of activation to define the “wet” state, so that droplets were initialized at the critical radius. Our method uses the 5% of water as a criterion so we can transfer aerosol particles to the unactivated state (or haze), allowing subsequent condensation to govern the evolution of the liquid droplet population. Once droplets in a bin evaporate to become smaller than the size of haze in equilibrium at 99% relative humidity, they are removed from the liquid spectrum. The maximum size of aerosol particles allowed to be “wet” is set to $10\mu\text{m}$, which excludes extremely giant aerosol particles from consideration.

c. Ice nucleation schemes

We investigate three immersion freezing ice nucleation schemes. Broadly speaking, these schemes represent the heterogeneous freezing of liquid droplets nucleated by insoluble particles inside the droplet. The first scheme is the volume-dependent freezing scheme “VF” used by [de Boer et al. \(2010, 2013\)](#). The other two schemes are based on classical nucleation theory (CNT), with consideration of the probability density function (PDF) of contact angles. “C-AC” is a scheme applied to activated cloud droplets only, and the other, “C-CM,” is applied to droplets containing coarse-mode aerosol particles only.

The VF scheme follows the stochastic hypothesis formulation by [Bigg \(1953\)](#). The number concentration of frozen droplets N_{fl}^b (cm^{-3}) in a time interval Δt (s) is given as

$$N_{fl}^b = N_l^b \left\{ 1 - \exp \left[-\frac{\bar{m}_l^b}{\rho_w} B \exp(aT_s) \Delta t \right] \right\}, \quad (1)$$

where N_l^b is the number concentration of droplets in the b th mass bin (cm^{-3}), \bar{m}_l^b is the mean mass of droplets in the bin (g), and ρ_w is the bulk density of liquid water (g cm^{-3}). Here, $T_s = T_0 - T$ ($^{\circ}\text{C}$), where T_0 is the reference temperature ($=0^{\circ}\text{C}$), and T is the temperature. [Diehl and Wurzler \(2004\)](#) expanded the volume-dependent freezing equation semiempirically to include the freezing-point depression ΔT_f due to soluble material in the droplets and the effect of insoluble aerosol particles based on laboratory experiments. If a constant cooling rate $\gamma_c = -dT/dt$ ($^{\circ}\text{C s}^{-1}$) is assumed, the freezing rate derived by [Diehl and Wurzler \(2004\)](#) [their Eq. (12)] can be integrated with respect to time to give the same form as Eq. (1) except T_s is replaced with $T_0 - T + \Delta T_f$. Finally, B ($\text{cm}^{-3} \text{s}^{-1}$) and a

($^{\circ}\text{C}^{-1}$) are freezing parameters and are assigned as $a = 1$ and $B = aB_{hi}\gamma_c$, with parameter B_{hi} (cm^{-3}) representing the freezing efficiency of the insoluble material immersed in the droplet. The freezing rate in this formulation strongly depends on the mass (or volume) of droplets in addition to B_{hi} and T .

The classical nucleation theory-based scheme used in this study follows the treatment of [Savre and Ekman \(2015, hereafter SE15\)](#) and reference therein. It includes the PDF of contact angles between ice and INPs, assuming that some fraction of droplets in a liquid mass bin contain the INPs governed by this PDF. For a given contact angle θ , the nucleation rate of ice crystals per unit surface area of immersion freezing mode can be written as

$$J_{\text{imm}} = A_{\text{imm}} \exp \left[\frac{-\Delta G_{\text{act,imm}} - \Delta G_{g,\text{imm}} f(\theta)}{kT} \right], \quad (2)$$

where A_{imm} is the pre-exponential factor, $\Delta G_{\text{act,imm}}$ is the activation Gibbs energy, $\Delta G_{g,\text{imm}}$ is the critical Gibbs energy for ice germ formation, $f(\theta)$ is the geometrical factor for ice germ formation on a planar surface, and k is Boltzmann’s constant. The formulas used for calculation of these variables are given in [appendix B](#). We introduce $p_{\text{imm}}(\theta)$, the PDF of θ , and the normalized particle size distribution of insoluble aerosol particles $f_a(r_N)$, where r_N is the radius of an insoluble aerosol particle. The number concentration of frozen droplets is obtained by integrating the number of particles nucleated over the plausible values of θ and r_N with $p_{\text{imm}}(\theta)$ and $f_a(r_N)$:

$$N_{fl}^b = \int_{\theta_{00}}^{\theta_{\text{max}}} \int_{r_{\text{min}}}^{r_{\text{max}}} F_{\text{inp}} N_l^b \times [1 - \exp(-4\pi r_N^2 J_{\text{imm}} \Delta t)] p_{\text{imm}}(\theta) f_a(r_N) d\theta dr_N, \quad (3)$$

where statistical independence of θ and r_N is assumed and F_{inp} is the fraction of the droplets that include immersed INPs.

We evaluate J_{imm} by using the aerosol mass components in each liquid mass bin. However, since the number of aerosol particles in each mass bin is not predicted, it is assumed that there is a single aerosol particle immersed in any liquid droplet. For instance, r_N is calculated for each mass bin with

$$r_N = \left(\frac{3}{4\pi\rho_{\text{api}}} \frac{M_{l,\text{apt}}^b - M_{l,\text{aps}}^b}{N_l^b} \right)^{1/3}, \quad (4)$$

where $M_{l,\text{apt}}^b$ and $M_{l,\text{aps}}^b$ are the mass-content components predicted for the total aerosol mass and soluble mass in

the b th mass bin, respectively. Also, ρ_{api} is the prescribed bulk density of insoluble material, which is set to 2.6 g cm^{-3} , the value for kaolinite. Equation (3) is integrated using the Gauss quadrature method, using eight nodes (N_θ) spanning the contact angles between θ_{00} and θ_{max} :

$$N_{\text{fl}}^b = \frac{1}{F_\theta(180^\circ) - F_\theta(0^\circ)} F_{\text{inp}} N_l^b \frac{\theta_{\text{max}} - \theta_{00}}{2} \times \sum_{i=1}^{N_\theta} [1 - \exp(-4\pi r_N^2 J_{\text{imm},i} \Delta t)] p_{\text{imm}}(\theta_i) w_i, \quad (5)$$

where w_i are the Gaussian weights and F_θ represents the cumulative distribution function of θ . The normalization factor $1/[F_\theta(180^\circ) - F_\theta(0^\circ)]$ is introduced because θ is defined between 0° and 180° . With the Gaussian point $x_{gq,i}$, $\theta_i = [(\theta_{\text{max}} - \theta_{00})x_{gq,i}/2 + (\theta_{\text{max}} + \theta_{00})/2]$. In Eq. (5), $(\theta_{\text{max}} - \theta_{00})/2$ appears due to the variable conversion necessary for the Gauss quadrature method. θ_{max} is set to 100° based on the result of SE15. By introducing a new PPV representing the number of INPs ($N_{l,\text{inp}}^b$) in a liquid mass bin, we determine F_{inp} as

$$F_{\text{inp}} = \frac{N_{l,\text{inp}}^b}{N_l^b}. \quad (6)$$

Here, $N_{l,\text{inp}}^b$ and the number of INPs within the aerosol spectra are specified at the initialization with a constant F_{inp} . Both F_{inp} and $N_{l,\text{inp}}^b$ are conserved during CCN transfer and vapor deposition. $N_{l,\text{inp}}^b$ of a bin is subtracted by N_{fl}^b as a result of the immersion freezing process [Eq. (5)]. SE15 proposed simulating the θ PDF to reflect the variability in INP efficiency and the quick removal of the most efficient INPs from the atmosphere. By introducing the number of activated INPs in a liquid mass bin $N_{l,\text{inact}}^b$ as a PPV, we find that

$$\theta_{00} = F_\theta^{-1} \left\{ \frac{N_{l,\text{inact}}^b}{N_{l,\text{inp}}^b} [F_\theta(180^\circ) - F_\theta(0^\circ)] + F_\theta(0^\circ) \right\}. \quad (7)$$

In this study, the PDF of θ is assumed to obey a normal PDF with mean $\bar{\theta}$ and standard deviation σ_θ , which were set to values representative of natural dust (132° and 20° , respectively) based on Table 1 of SE15.

In the C-AC version of this scheme, F_{inp} is set to 1 (all droplets contain INPs) and freezing is applied to activated droplets only. This is motivated by the definition of “immersion freezing” dealing only with activated droplets in a traditional sense. In the C-CM version of this immersion freezing scheme, F_{inp} is set to a small value (only some droplets contain INPs) and only applied to liquid droplets containing aerosol particles with average diameter exceeding $0.5 \mu\text{m}$. This version is consistent

with airborne observations north of Utqiagvik, Alaska (formerly Barrow), showing that only a small fraction of aerosol particles contain dust (Lance et al. 2011; Liu et al. 2011). The $0.5\text{-}\mu\text{m}$ size requirement is consistent with previous findings (DeMott et al. 2010).

In summary, the VF scheme considers the volume of droplets, air temperature, and molality irrespective of the state of activation of droplets, and Eq. (1) is applied to all droplets similarly (Fig. 1a). The C-AC scheme only targets activated droplets with the assumption that all droplets contain INPs, and the freezing rate is a function of air temperature, supersaturation, molality, size of INPs, and the contact angle PDF (Fig. 1b). The C-CM scheme uses the same freezing rate as that in the C-AC scheme, but is applied to droplets that contain aerosol particles larger than $0.5 \mu\text{m}$, irrespective of activation status (Fig. 1c).

d. Experiment design

We selected a stratiform mixed-phase cloud observed on 7 May 1998 during the Surface Heat Budget of the Arctic (SHEBA) cruise (Uttal et al. 2002). In this case, the surface latent and sensible heat fluxes are relatively weak due to a surface sea ice covering and most of the observed ice particles are unrimed crystals, a situation that allows us to focus on ice nucleation and vapor deposition processes. We follow the forcing and initial conditions specified by the Global Energy and Water Cycle Experiment (GEWEX) Cloud System Study (GCSS) SHEBA model intercomparison (Morrison et al. 2011). The surface latent heat flux over sea ice is set to 2.86 W m^{-2} , the sensible heat flux to 7.98 W m^{-2} . The horizontal winds are nudged to the initial profiles with a relaxation time of 1 h. Additionally, we included subsequent adjustments implemented by Fridlind et al. (2012, hereafter F12) on initial temperature and moisture profiles to represent the 1800 UTC sounding. Unlike study F12, we do not specify any large-scale moisture advection, but we do keep the large-scale temperature advection term the same as in the original GCSS intercomparison. Simulations begin with the supercooled liquid layer as done in the intercomparison and run for 4 h with the first 2 h being a spin-up period. Ice processes are turned on from the beginning together with the liquid processes.

We use a domain size of $3.2 \text{ km} \times 3.2 \text{ km} \times 1 \text{ km}$ (1-km height) with double periodic boundary conditions. Horizontal resolution is set to 50 m, with a constant vertical resolution of 10 m. We chose the sizes based on feasibility of sensitivity experiments under the computational power required for AMPS and also to follow the F12 setting for comparison. The dynamics time step is set to 2 s, and further divided into 10 sub-time steps for the calculation of cloud microphysical processes. A 0.2-s sub-time step is used to solve for supersaturation and vapor-deposition processes, whereas a 2-s time step

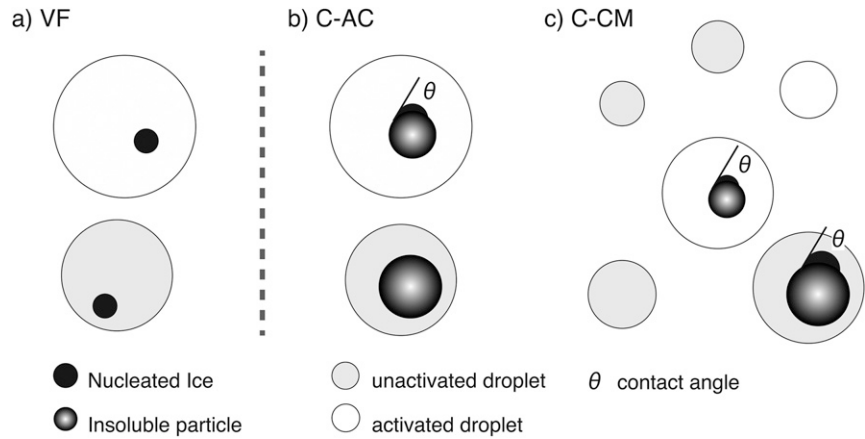


FIG. 1. The three immersion freezing schemes. (a) VF and (b) C-AC assume that all droplets contain a single INP. (c) C-CM assumes a small fraction of droplets contain a single INP. VF calculates the freezing rate for all droplets irrespective of the activation state. C-AC calculates the freezing rate only for activated droplets, ignoring unactivated droplets. C-CM calculates the freezing rate only for droplets containing aerosol particles larger than $0.5\text{ }\mu\text{m}$, irrespective of activation state. VF does not use information of INP simulated in SHIPS, but the parameters are specified.

is used for collection processes. Forty and 20 mass bins are defined for liquid and ice particles, respectively (Table 2), following the previous studies with AMPS (Hashino and Tripoli 2007, 2008; de Boer et al. 2010, 2013). Two categories of condensation nuclei are specified to represent the Aitken mode and accumulation/coarse mode (hereafter CRS mode) with lognormal size distributions, both made up of NH_4HSO_4 accounting for 70% of the soluble mass fraction (see de Boer et al. 2013). For simplicity, the number concentration and mass content of dry aerosol particles in the two aerosol categories are not reduced after “wet” transfer. The number of droplets is constrained based on the observed value (215 cm^{-3}) in the “wet” transfer process.

Six base cases are considered to evaluate any links between immersion freezing and habit within the uncertainty of the LWP observation (Table 3). LWP is closely related to the variance of vertical motions through cloud-top radiative cooling, which is thus the

driver of the cloud dynamics. The simulations include two variations of the VF immersion freezing parameterization, VF14 and VF10, with both assuming a constant cooling rate $\gamma_c = 10^{-2}\text{ }^\circ\text{C s}^{-1}$. The cooling rate of air parcels in a liquid cloud layer equals the moist adiabatic lapse rate Γ_m times the vertical velocity w , or $\gamma_c = \Gamma_m w$. As $\Gamma_m \cong 8.5 \times 10^{-3}\text{ }^\circ\text{C m}^{-1}$ at -18°C , the above cooling rate corresponds to an updraft of 1.2 m s^{-1} (almost equal to the maximum updraft simulated in this study). VF14 sets $B = 4.7 \times 10^{-8}\text{ cm}^{-3}\text{ s}^{-1}$ (Table 3), which corresponds to a $B_{h,i}$ that is a weighted average of the $B_{h,i}$ from montmorillonite (14.4%) and kaolinite (85.6%). In contrast, for VF10 the $B_{h,i}$ is a weighted average from 10% montmorillonite and 90% kaolinite, giving a smaller B of $3.2 \times 10^{-8}\text{ cm}^{-3}\text{ s}^{-1}$ to simulate a lower freezing rate than VF14. Although the constant cooling rate assumption removes the dependency on vertical velocity, we adopt this assumption to be consistent with our previous studies (de Boer et al. 2010, 2013).

TABLE 2. Definition of mass bin boundaries. N denotes the number of mass bins. The left mass boundary of a b th bin m_1^b is calculated with $m_1^b = k_{bb}^b m_1^{b-1}$. For the liquid phase, the radii of the spheres corresponding to the smallest and largest masses are shown in parentheses. For the ice phase, the a -axis lengths of a hexagonal column are in parentheses, which were calculated with bulk density of ice and axis ratio of 1.

Phase	Group	N	k_{bb}^b	Smallest mass	Largest mass
Liquid	Deposition growth	20	2.29	$4.19 \times 10^{-15}\text{ g}$ ($0.1\text{ }\mu\text{m}$)	$6.54 \times 10^{-8}\text{ g}$ ($25\text{ }\mu\text{m}$)
	Collection growth	20	2.21	$6.54 \times 10^{-8}\text{ g}$ ($25\text{ }\mu\text{m}$)	$5.24 \times 10^{-1}\text{ g}$ (5 mm)
Solid	Deposition growth	4	22.1	$4.19 \times 10^{-12}\text{ g}$ ($0.96\text{ }\mu\text{m}$)	$1.0 \times 10^{-6}\text{ g}$ ($59.4\text{ }\mu\text{m}$)
	Collection growth	10	2.51	$1.0 \times 10^{-6}\text{ g}$ ($59.4\text{ }\mu\text{m}$)	$1.0 \times 10^{-3}\text{ g}$ ($594\text{ }\mu\text{m}$)
	Riming growth	6	3.16	$1.0 \times 10^{-3}\text{ g}$ ($594\text{ }\mu\text{m}$)	$1.0 \times 10^1\text{ g}$ (1.28 cm)

TABLE 3. Summary of experiment cases.

Expt	Description
VF14	Volume-dependent stochastic immersion freezing scheme (Diehl and Wurzler 2004); B set to $4.7 \times 10^{-8} \text{ cm}^{-3} \text{ s}^{-1}$
VF10	As in VF14, but with B set to $3.2 \times 10^{-8} \text{ cm}^{-3} \text{ s}^{-1}$
C-AC7	Classical-nucleation-theory-type scheme that simulates PDF of contact angles (SE15); uses natural dust; θ_{00} of dry aerosol particles set to 60.3° ; F_{inp} set to 1
C-AC9	As in C-AC7, but with θ_{00} set to 60.9°
C-CM2	Classical-nucleation-theory-type scheme that simulates PDF of contact angles (SE15); uses natural dust; θ_{00} of dry aerosol particles set to 0° ; F_{inp} set to 0.02
C-CM07	As in C-CM2, but with F_{inp} set to 0.007
Diag-PL	As in VF14, but mass–dimensional relationship and axis ratio specified with empirical equations for P1a from Auer and Veal (1970)
No-CLL	As in VF14, but collision–coalescence of liquid hydrometeors excluded
No-CRS	As in VF14, but the coarse mode of aerosol particles excluded

The simulations also include two variations of the C-AC model. Here, C-AC7 and C-AC9 use different minimum contact angles θ_{00} , with θ_{00} of C-AC7 being slightly smaller (Table 3). In the initial supercooled cloud layer, the number of activated INPs in liquid mass bins $N_{i,\text{inact}}^b$ is initialized by setting $N_{i,\text{inact}}^b/N_{i,\text{inp}}^b$ equal to 7×10^{-4} and 9×10^{-4} for C-AC7 and C-AC9, respectively. This corresponds to $\theta_{00} = 60.3^\circ$ and 60.9° . Similarly, the number of activated INPs in the aerosol categories is prescribed to these values.

For the two C-CM schemes, θ_{00} is initialized to 0 for the liquid mass spectrum (prescribed to 0 for the aerosol categories). The value of F_{inp} is initialized to 0.02 for C-CM2 and 0.007 for C-CM07 in the initial cloud layer (prescribed to the values for the aerosol categories). These values correspond to 36- and 12.6-L^{-1} concentrations of INP, which are close to the observed mineral dust concentrations for clean Arctic environments (Lance et al. 2011).

The above nucleation parameters for all three schemes were selected (or tuned) so as to simulate a realistic range of LWP, IWP, and radar reflectivity distributions.

Three more sensitivity experiments are considered to clarify effects of using a fixed mass–dimensional relationship and to investigate an origin of large drops (Table 3). Diag-PL calculates a - and c -axis lengths based on the mass–dimensional relationship and axis ratio of P1a from Auer and Veal (1970) for given ice crystal mass. In No-CLL we remove the collision–coalescence process for liquid hydrometeors, while in No-CRS we remove the CRS mode aerosol category from the simulation. The same freezing scheme as that in VF14 is implemented in the three cases.

e. Calculation of radar reflectivity

During the SHEBA campaign, a Ka-band millimeter-wavelength cloud radar (MMCR; Shupe et al. 2001) was operated to provide vertical profiles of radar reflectivity, mean Doppler velocity, and spectral width of Doppler velocity. Our simulations here are compared to only the

radar reflectivity data. Synthetic radar reflectivities were calculated with the EarthCARE active sensor simulator (EASE) (Okamoto et al. 2003, 2007, 2008; Nishizawa et al. 2008) installed in the joint simulator for satellite sensors (Joint-Simulator; Hashino et al. 2013). EASE can be configured to simulate either a ground-based or space-borne radar. The joint simulator is equipped with a nonspherical scattering database for ice particles (Joint Simulator Scattering Database), and the simulated ice particle types and habits for each mass-spectrum bin are directly used to specify scattering models. The correspondence between ice particles and scattering models come mainly from data sources in Liu (2008) and Ishimoto (2008) for the Ka band (Table 4). Because the particle type and crystal habit diagnosed in AMPS are not exactly the same as those available in the scattering database, the single scattering parameters are tabulated in terms of an equivalent spherical volume radius (Okamoto 2002). Then, we construct lookup tables for each scattering model to evaluate single scattering parameters for each mass bin. Inside of a mass bin, the scattering parameters are calculated at 50 discrete mass points linearly spaced on a logarithmic scale, which are then summed with specification of a uniform distribution and number concentration of 1 cm^{-3} . For comparison, another lookup table is constructed using the Mie approximation in which the equivalent spherical volume radius is used to calculate the size parameter and cross-section area. The dielectric constant of water $|K_w|^2$ is set to 0.93 to obtain the equivalent radar reflectivity factor (Maahn and Löhnert 2017). Whereas SHIPS and Spectral Liquid Prediction System (SLIPS) assume subgrid piecewise linear or cubic polynomial mass distributions for microphysical calculations, EASE assumes uniform mass distributions. Therefore, a discrepancy occurs in the representation of mass distributions that will be investigated in the future.

TABLE 4. Nonspherical scattering database of ice particles and corresponding habit of ice particles. Scattering data with an asterisk (*) are from Ishimoto (2008), and all the others are from Liu (2008). ϕ is the axis ratio of hexagonal plates.

SHIPS diagnosis			Scattering model	
Type	Habit		Shape	Range of maximum dimension (μm)
Pristine and rimed crystals	Plates	$\phi < 0.1$	Thin plate	$\phi = 0.05$ 127–5059
		$0.1 < \phi < 0.8$	Thick plate	$\phi = 0.2$ 81–3246
		$0.8 < \phi$	Block column	$\phi = 1$ 66–2532
			Thick plate	$\phi = 0.2$ 81–3246
Pristine and rimed crystals	Planar polycrystals		Bullet rosettes with six branches	50–10 000
Pristine and rimed crystals	Irregular polycrystals		3D fractal particles with fractal dimension $d_f = 2.1^*$	1135–20 000
Aggregates	Any		Bullet rosettes with six branches	50–10 000
Graupel	Any		Mie with melt equivalent	—
Frozen drops	Any			

3. Results

a. Time series

All of the simulations completed under the six cases (VF, C-AC, and C-CM) maintained a domain-average LWP over the course of simulation (Fig. 2), and the LWP during the last 2 h falls within the $5\text{--}10\text{ g m}^{-2}$ range presented in F12 (their Fig. A3, at 2200–2400 UTC). The LWP of VF10, C-AC9, and C-CM07 increase with time after 1 h of simulation, whereas the other cases show a slight decrease over time. The simulated IWPs reflect the ice nucleation efficiencies; namely VF14, which assumes a greater $B_{h,i}$ value, produces more IWP than VF10, whereas the IWP of C-AC9 is smaller than C-AC7 due to the slightly larger θ_{00} . The N_d time series fluctuates the most, but the relative magnitudes of the cases resembles that with LWP. For instance, VF14 indicates smaller values than C-CM2 for LWP as well as for N_d . Due to the small number concentrations of ice particles, little aggregation occurs in these simulations, and thus the immersion freezing results in an inverse relationship between N_d and N_i . We also find that the domain-average freezing rate in the cloud layer varies between 0.11 and $0.89\text{ L}^{-1}\text{ h}^{-1}$ (Table 5), depending on the scheme, which is reflected on the time series of N_i .

b. Spatial habit distribution

Habits predicted for 7 May 1998 case include hexagonal plates, irregular polycrystals, planar polycrystals, and frozen droplets. Most of the simulated ice particles are pristine crystals due to the low amounts of riming and aggregation. These habits agree with observations from this case (F12). Figure 3 shows vertical profiles of temperature T , relative humidity with respect to water, and relative humidity with respect to ice at model initialization (dashed) and during the last 2 h of simulation. These profiles show a well-mixed lower atmosphere

between cloud top and the surface, with slow cooling at lower levels. The cloud layer extends from approximately 250–400 m. During the last 2 h of simulation, the atmosphere below cloud base is supersaturated with respect to ice, meaning that precipitating ice crystals do not sublimate.

For case VF14, the number concentrations of plates, irregular polycrystals, and frozen droplets are shown in

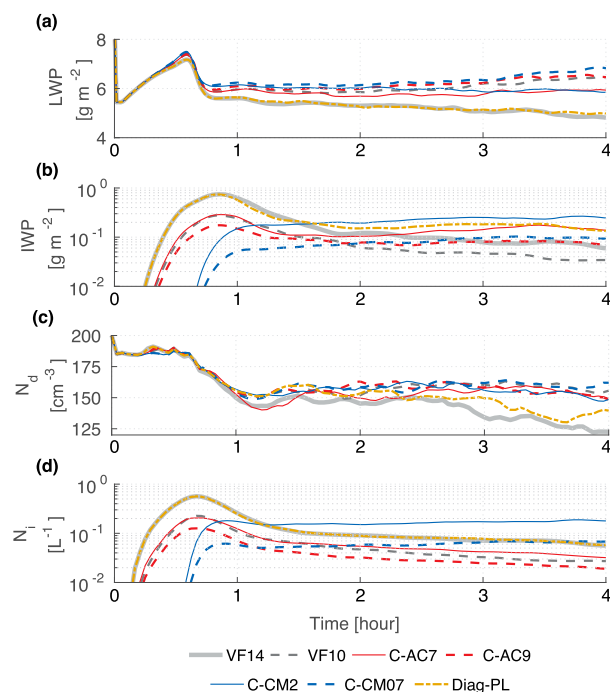


FIG. 2. Domain-averaged time series for VF, C-AC, C-CM, and Diag-PL cases. (a) Liquid water path. (b) Ice water path. (c) Number concentration of cloud droplets. (d) Number concentration of ice particles. Following F12, N_d is based on droplets with $1 < D < 50\text{ }\mu\text{m}$ and grid boxes with liquid mixing ratio exceeding 10^{-3} g kg^{-1} .

TABLE 5. Freezing rates ($L^{-1} h^{-1}$) averaged based on vertical velocity regimes in the cloud layer ($230 < z < 450$ m) during the last 2 h. Averages were calculated over the grids with freezing events occurring and those irrespective of freezing events over the domain.

		VF14	VF10	C-AC7	C-AC9	C-CM2	C-CM07
Averages with freezing events	Downdraft	0.56	0.27	0.36	0.21	0.28	0.11
	Updraft	0.43	0.19	0.64	0.36	2.22	0.81
Averages irrespective of freezing events	Downdraft	0.44	0.22	0.12	0.07	0.21	0.08
	Updraft	0.34	0.15	0.26	0.15	1.66	0.62
Total		0.40	0.19	0.18	0.11	0.89	0.33

vertical slices in the top row of Fig. 4. Similar slices for cloud droplets ($1 < D < 50 \mu m$) and large droplets ($30 < D < 100 \mu m$) are shown in the bottom row along with the vertical velocities. The plates are vertically distributed throughout the cloud layer and below it, indicating that they represent the bulk of the precipitating ice crystals. Irregular polycrystals occur in high number concentrations mainly near cloud top, but also below the cloud base in areas of downdrafts. Frozen droplets also occur near the cloud tops and in the middle of the cloud layer, though in much lower concentrations than the other two crystal types. We find in section 3c that these two regions (cloud top and midcloud) are related to two separate size populations of cloud droplets at the time of freezing.

Horizontal cross sections of the cloud reveal additional relationships between ice crystal habits and vertical velocities. Figure 5 shows midcloud sections at $z = 350$ m of the various habit concentrations. The areas of high concentration of plates are distributed in a cellular fashion, with the locations of these cells generally

corresponding to the locations of updrafts. For instance, consider the box marked “A” in Fig. 5f, a region with peak updrafts. This box, as also marked in Fig. 5a, has some of the highest concentrations of hexagonal plates. In a lower cross section at $z = 300$ m, box “B” in Fig. 6b shows high concentrations of irregular polycrystals spread out in a somewhat banded pattern, a pattern that matches regions of negative vertical velocities (bluish color in Fig. 6f). Finding more irregular polycrystals in downdrafts is consistent with our findings discussed above about Figs. 4b and 4f (e.g., box “C”). These findings suggest that the relations between habit and updraft may also depend on the vertical position within the cloud.

To examine relationships between habit, updraft, and height within the cloud more quantitatively, we used the gridpoint values to calculate averages and percentiles of number concentrations for plates and irregular polycrystals. Results in Fig. 7 show that the averages and medians of plate number concentrations tend to increase with updraft speed in the lowest three layers,

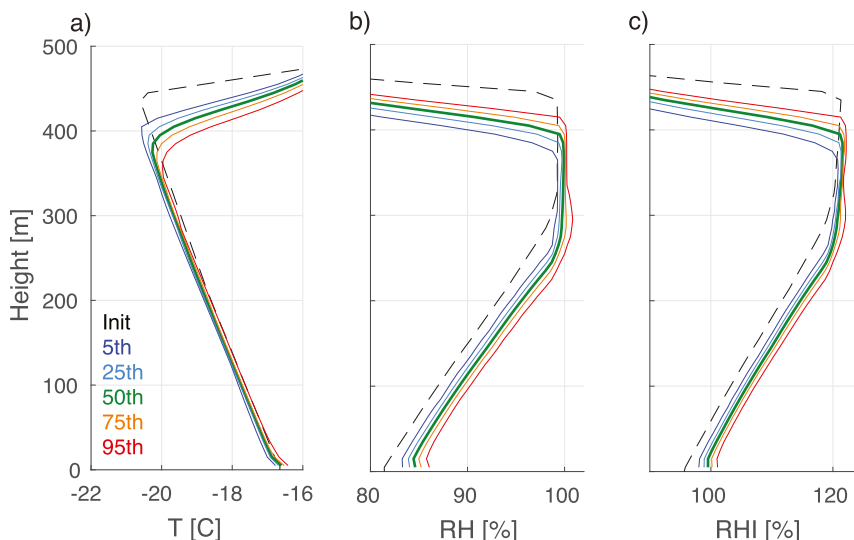


FIG. 3. Vertical profiles of thermodynamic variables for VF14. (a) Temperature. (b) Relative humidity over water. (c) Relative humidity over ice. Initial profiles are dashed lines. Solid lines indicate the 5th, 25th, 50th, 75th, and 95th percentiles, all during the last 2 h of simulation.

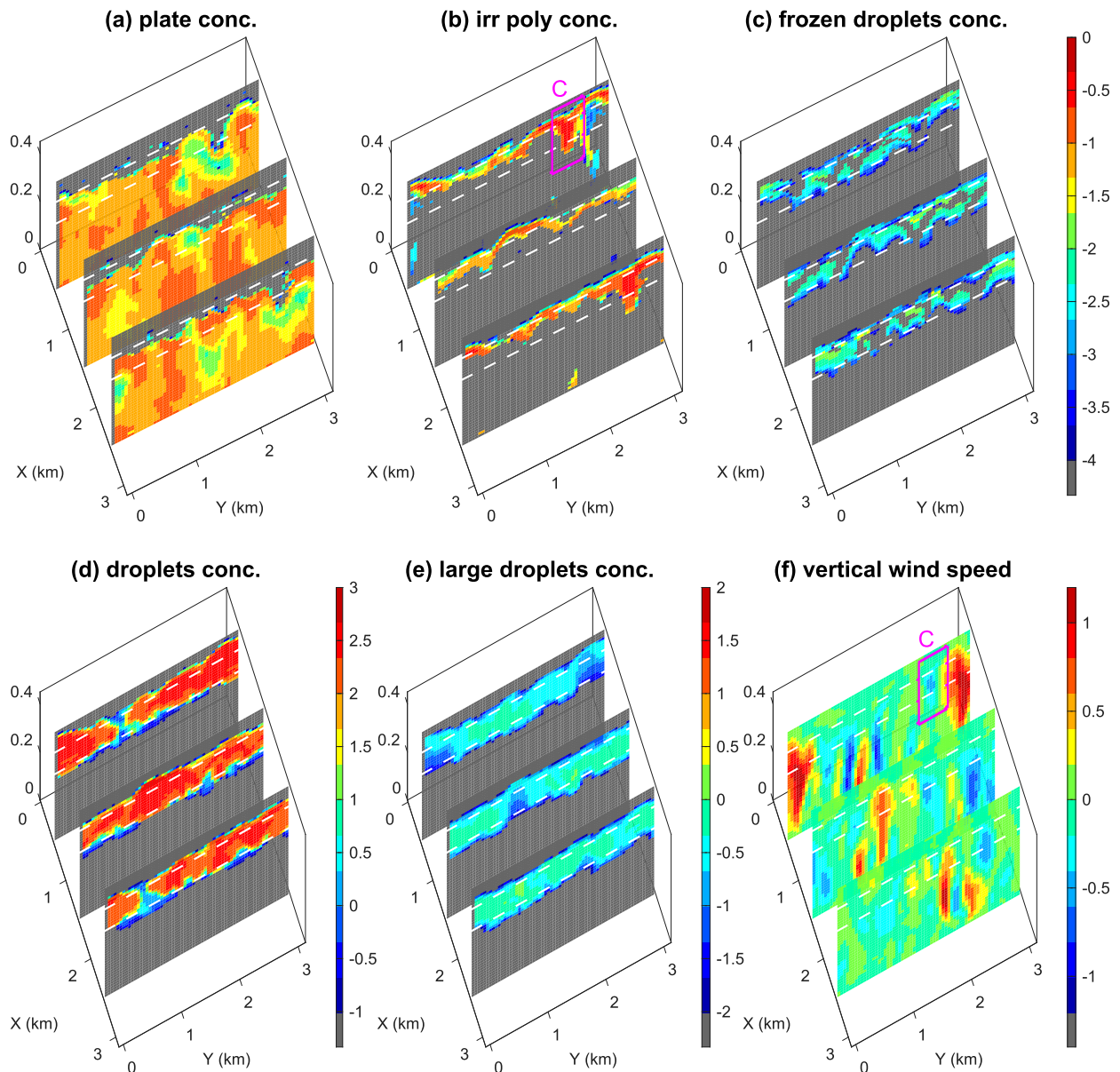


FIG. 4. Vertical slices of number concentrations and updrafts in the simulated cloud after 3 h, case VF14. (a) Plates. (b) Irregular polycrystals. (c) Frozen droplets. (d) Cloud droplets. (e) Large droplets. (f) Updraft speed. The slices are located at $x = 0.5, 1.5$, and 2.5 km. The units are (a)–(c) $\log_{10}(\text{L}^{-1})$, (d),(e) $\log_{10}(\text{cm}^{-3})$, and (f) m s^{-1} . Box C indicates a location where irregular polycrystals are collocated with downdrafts. The white dashed lines are average cloud-top and cloud-bottom boundaries defined by domain average $\text{RH} \geq 100\%$.

whereas those of irregular polycrystals increase with downdraft speed in these layers (Figs. 7a–c). However, these relationships do not hold at cloud top (Fig. 7d). In the lower parts of the cloud, the medians of habit concentrations also show a reverse relationship, with the median plate concentration slightly increasing with downdraft speed at the cloud bottom (Fig. 7a) and the median concentration for irregular polycrystals increasing with updraft speed in the lowest two layers (Figs. 7a,b).

The correspondence between the presence of irregular polycrystals and sinking air comes from SHIPS. In SHIPS, polycrystals form only when T is below -20°C . The vertical profile of median temperature in Fig. 3a shows that temperatures below -20°C are mostly reached between 340 and 400 m. For the simulated range of T (up to -20.5°C) and RHI ($\sim 120\%$), polycrystals occur in 60%–70% of the nucleation events, with irregular polycrystals forming in about 70% of these cases, planar

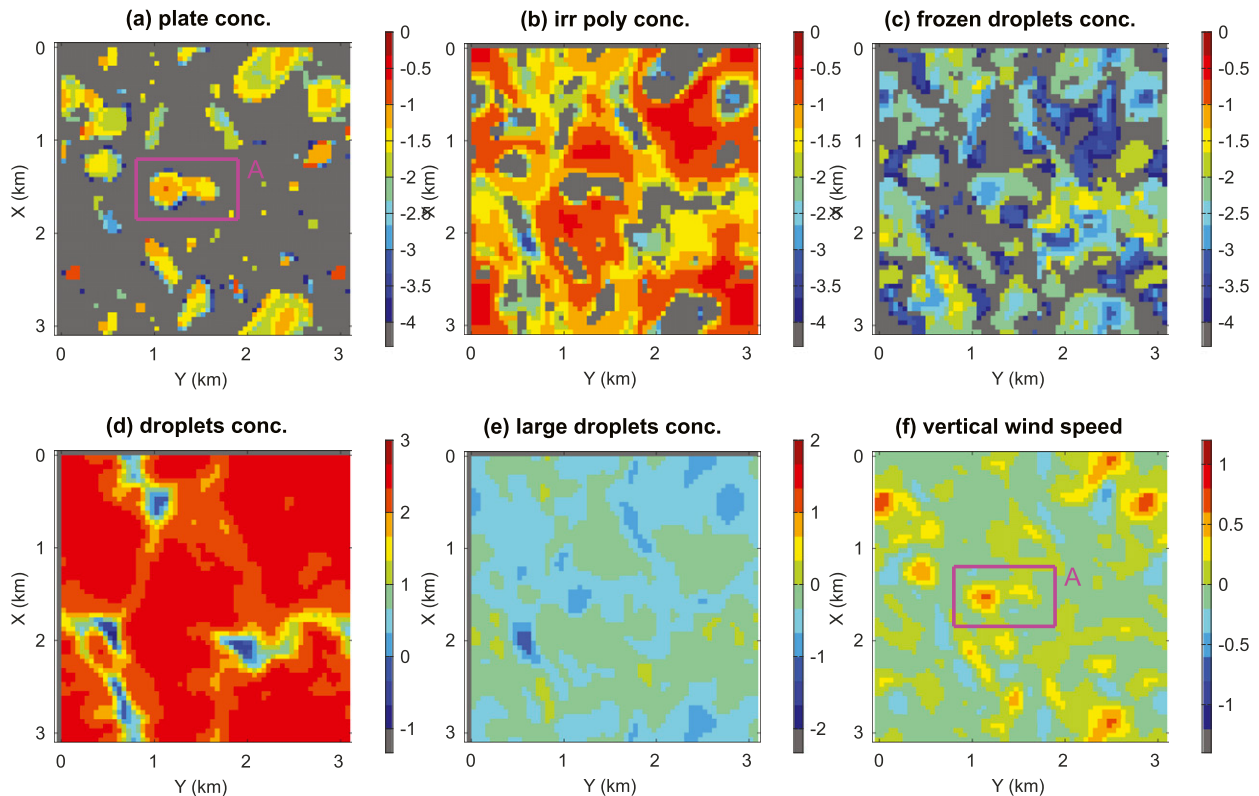


FIG. 5. As in Fig. 4, but for a horizontal slice at $z = 350$ m. Box A indicates a location where plates are collocated with updrafts.

polycrystals forming in the remaining 30% (see Fig. 1 of Hashino and Tripoli 2008). Therefore, crystals are mostly diagnosed to be irregular polycrystals at the time of initiation for T ($\sim -20.5^{\circ}\text{C}$) and RHI ($\sim 120\%$). After a crystal grows to $20\text{ }\mu\text{m}$, its habit is determined. The time required to grow from the size of a frozen droplet ($\geq 10\text{ }\mu\text{m}$, section 3c) to $20\text{ }\mu\text{m}$ is rather short, so the habits are generally determined by the habit at the time of ice crystal nucleation near the cloud top. These cloud-top crystals are subsequently advected downward toward warmer temperatures by downdrafts in the cloud. An occasional high concentration of irregular polycrystals also can occur in updrafts (Fig. 7), which suggests that advected irregular polycrystals can re-enter updraft regions before precipitating all the way to the surface.

The cellular structure of plate concentrations in the updraft region suggests that many of the plates form in the updraft regions. As shown in the next section, we find that plates also nucleate in the downdraft regions inside the cloud, then re-enter from cloud base. In SHIPS, hexagonal plates can form in the whole temperature range shown in Fig. 3a, with the inherent growth ratio being less than 1 (planar growth) at T between -20° and -10°C .

The above trends between habits and vertical velocities occur in the other immersion freezing cases. For

example, in C-AC9, irregular polycrystals mostly exist near the cloud top and in downdrafts between areas of high droplet concentration (Figs. 8b,d,f). The horizontal distribution of plate number concentrations at $z = 300$ m clearly indicates a cellular structure, whereas those of irregular polycrystals display the band-like structure (Figs. 9a,b). These structures are mostly related to updraft and downdraft areas (Fig. 9f), as seen for VF14. However, vertical slices of number concentrations for plates show a maximum near the cloud top and appear to be related to high concentrations of cloud droplets (Figs. 8a,d). This qualitatively differs from VF14, where plates occur in high concentrations both inside and below the cloud layer.

The horizontally averaged number concentrations of individual crystal habits depend on the ice nucleation scheme. All the cases show a well-mixed concentration of plates below about 325 m, the center of the mixed-phase cloud layer (Fig. 10). The VF simulations feature a dominance of irregular polycrystals above about 325 m, whereas the other cases indicate a mixed state of plate and irregular polycrystals near the cloud top. Planar polycrystal concentrations are highest in the C-AC simulations, but relatively low compared to the other habits for all simulations. Concerning

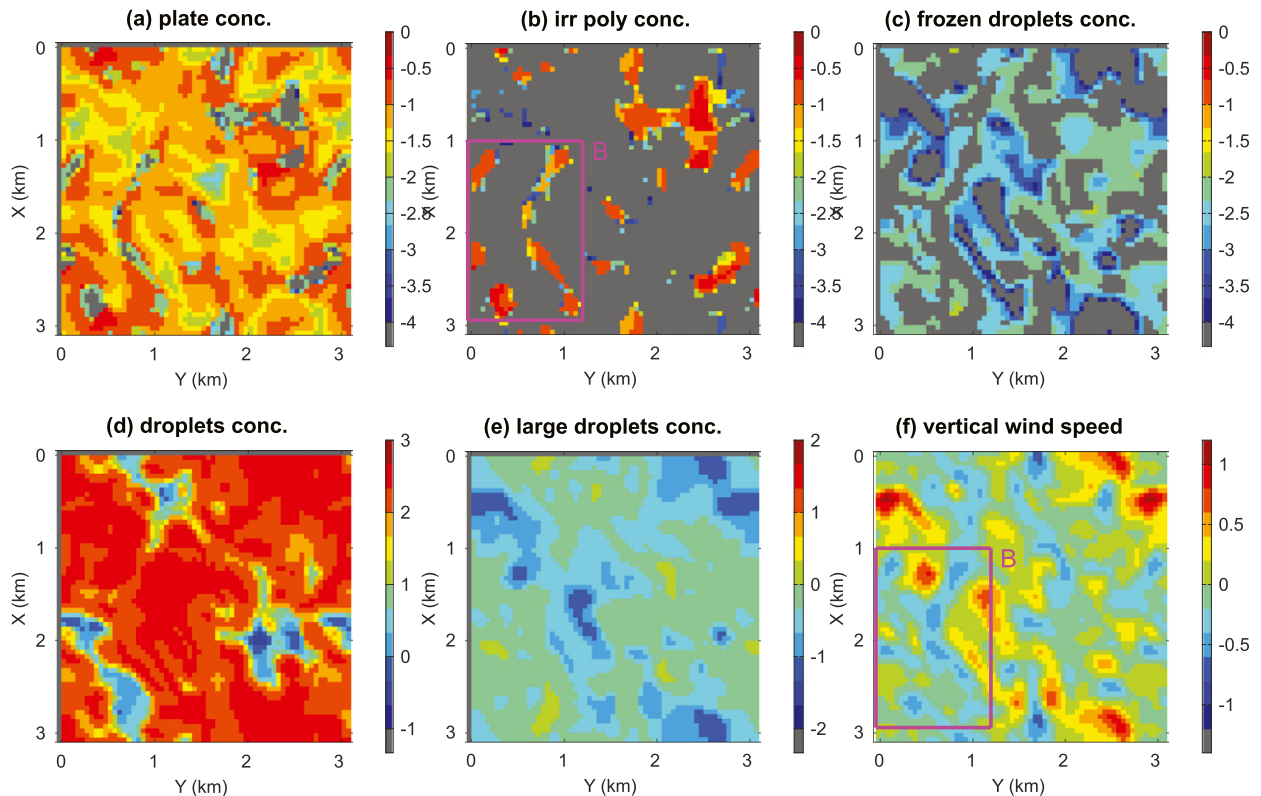


FIG. 6. As in Fig. 5, but for a slice is at $z = 300$ m. Box B indicates a location where irregular polycrystals are collocated with downdrafts.

the frozen spheres, this habit occurs in the VF simulations throughout the depth of the mixed-phase layer, whereas the C-AC simulations have them only above 320 m and the C-CM simulations have a bimodal structure, with one peak near the top and another near the base. These differences between the simulations are attributed to the location of active freezing processes as discussed in the next section.

c. Relationships between cloud droplets and freezing nucleation

The VF simulations show how the highest nucleation rates relate to the highest number concentration of large cloud droplets outside of updraft centers. Regions of elevated cloud droplet concentrations N_c are generally collocated with weak to moderate updrafts (Figs. 5d,f and 6d,f). In the case of VF14, quantiles of N_c for a given updraft speed W tend to increase with W , but clouds with $N_c = 230 \text{ cm}^{-3}$ are concentrated around zero vertical velocity (Fig. 11a). As the number concentration of liquid droplets is constrained to be less than 215 cm^{-3} in the wet transfer process, horizontal convergence of the number flux probably increases the concentration to 230 cm^{-3} . On the other hand, liquid droplets of diameter over $30 \mu\text{m}$ occur outside the updraft cores, favoring

weak to moderate downdraft cores (Figs. 5e,f and 6e,f). According to the joint PDF of W and large droplet number concentration $N_{c,\text{large}}$ (Fig. 11b), there is a mode near downdrafts and a weak negative correlation with W . Indeed, the average $N_{c,\text{large}}$ in downdrafts is 0.32 cm^{-3} , which is larger than that in updrafts (0.19 cm^{-3}). The horizontal convergence of droplet number concentration flux is positive in $-0.5 < W < 0.1 \text{ m s}^{-1}$ on average, which contributes to the peak of $N_{c,\text{large}}$ in downdraft regions. The collocation of large droplets with downdrafts is probably due to shallowness of the cloud layer and weak updrafts that reduce the condensation rate.

Characteristics of the three immersion freezing schemes (VF, C-AC, and C-CM) can be seen in the dependence of freezing rate on droplet diameter and height. For this comparison, the simulated freezing rates were accumulated over the last 2 h of simulation in the diameter–height space and then divided by the sum of the accumulated freezing rates to obtain normalized freezing rates in Fig. 12. The top row shows the normalized freezing rates in downdrafts; the bottom row shows that for updrafts.

For VF14 (left column), one freezing mode occurs near the cloud top ($z > 350$ m) with $D \sim 10 \mu\text{m}$, both in

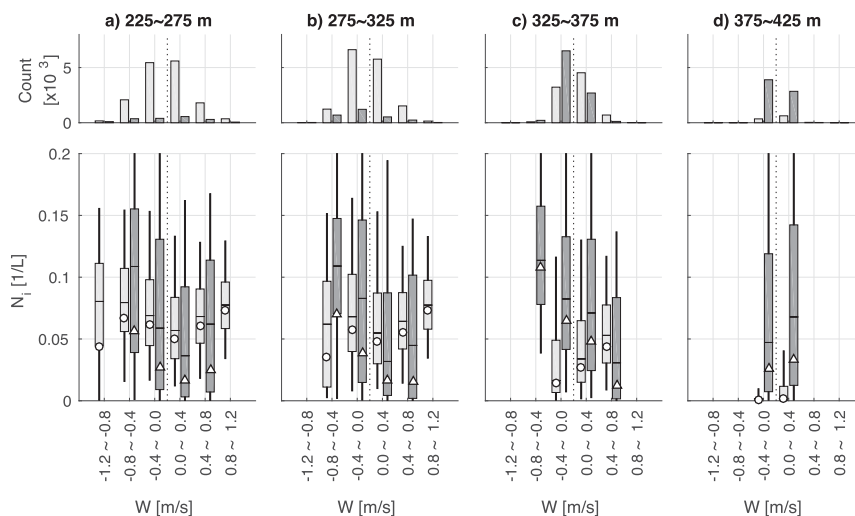


FIG. 7. Vertical motions and (bottom) number concentration and (top) number of samples for the last 2 h of simulation with VF14 at four altitudes increasing from (a) to (d). Each vertical velocity range on the horizontal axis contains a pair of box plots corresponding to statistics for hexagonal plates (light gray boxes) and for irregular polycrystals (dark gray boxes). The box plots indicate 95th, 75th, median, 25th, and 5th percentiles. The white circles and triangles indicate averages calculated in logarithms. Only grid boxes with number concentration exceeding 10^{-4} L^{-1} were included in the statistics.

up- and downdrafts. There are two additional modes at larger droplet sizes (around 18 and $32 \mu\text{m}$), which are more homogeneously distributed in the upper half of the cloud layer. The combination of a higher freezing rate of large droplets and the larger number of large droplets in the downdrafts leads to more ice nucleation in downdrafts. The average freezing rate, including all droplet sizes, in the downdraft regions is 0.56 and $0.43 \text{ L}^{-1} \text{ h}^{-1}$ for updrafts. The corresponding numbers for VF10 are 0.27 and $0.19 \text{ L}^{-1} \text{ h}^{-1}$ (Table 5). As the volume fraction of downdraft regions is 53% (similar for all cases), the domain-averaged rate of ice nucleation in downdrafts is also larger than that in updrafts (Table 5).

The C-AC cases have a high freezing rate in areas with a high concentration of cloud droplets. In C-AC9, the relationships between cloud droplets, large cloud droplets, and vertical velocities are similar to those of VF14 (Fig. 9); however, the normalized freezing rate of C-AC9 shows a maximum rate between 8 and $10 \mu\text{m}$ in the upper cloud layer and no mode connected to the freezing of large cloud droplets (Figs. 12b,e). Furthermore, the nucleation rates in updrafts indicates freezing of even smaller cloud droplets (down to a few micrometers) in the lower parts of the cloud. Overall, the average freezing rates for C-AC9 in updrafts ($0.36 \text{ L}^{-1} \text{ h}^{-1}$) are larger than those in downdrafts ($0.21 \text{ L}^{-1} \text{ h}^{-1}$). In contrast to that in the VF cases, the domain-average freezing rate in updrafts is larger than that in downdrafts.

The C-CM cases indicate a stronger dependence of freezing rate on updraft. The general features shown in Fig. 12 for C-CM07 (right column) apply to both C-CM cases. In updrafts, three significant modes of freezing occur near cloud base (isopleth larger than -2 in Fig. 12f), with the largest mode near diameters of $15 \mu\text{m}$, the middling mode for droplets around $25\text{--}32 \mu\text{m}$, and the smallest mode for $8\text{--}10\text{-}\mu\text{m}$ -sized droplets. Similarly, three modes occur near the cloud top with freezing rates one order of magnitude smaller than those near cloud base. In downdrafts, only two significant modes exist, occurring near the cloud top with droplet diameters near 8 and $15 \mu\text{m}$ (Fig. 12c). The resulting average freezing rate is 8 times larger in updrafts than in downdrafts (0.81 vs $0.11 \text{ L}^{-1} \text{ h}^{-1}$ for C-CM07). The same holds for the domain averages. The reason for the difference is related to supersaturation being larger in updrafts than in downdrafts, resulting in about 50 times larger transfer rates of aerosol particles into the liquid spectrum as discussed in section 4c.

d. Comparison of radar signals between simulations and MMCR observations

We now ask if any of the three schemes produce a realistic distribution of radar reflectivity. As noted in section 2d, the current study tuned the parameters related to the efficiency of freezing to ensure realism in the simulation. Therefore, discussion is focused on features pertaining to the schemes instead of speculating the best

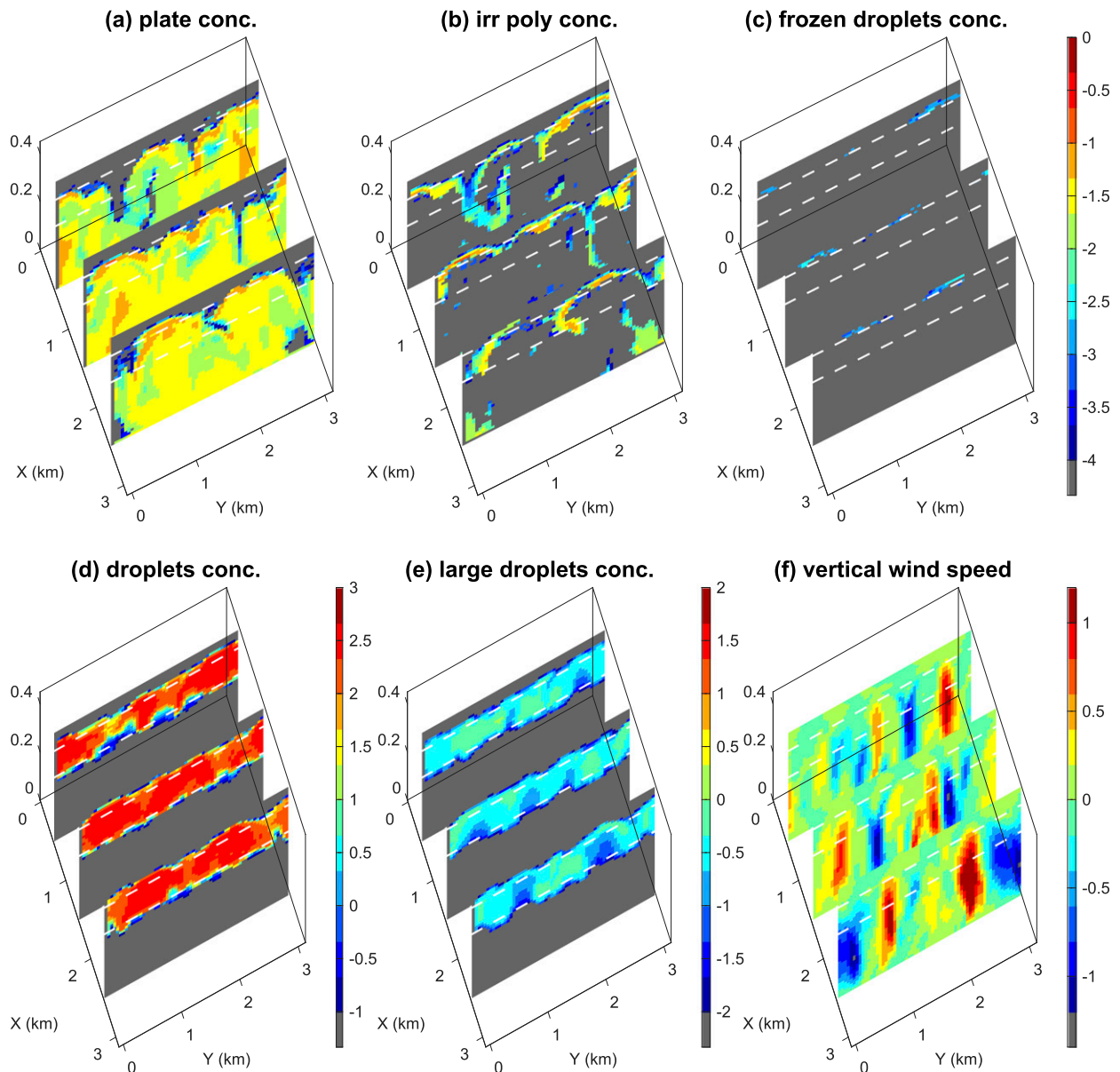


FIG. 8. As in Fig. 4, but for C-AC9.

scheme among the three. Following F12, ice particles below cloud base ($82.5 < z < 217.5$ m) are extracted to construct histograms of radar reflectivity (Fig. 13). The focus on the region below cloud is because here the in situ measurements of ice particle size distributions and habits were available.

Qualitatively, the frequency and median of the simulated radar reflectivity roughly fit observations. However, using the Mie reflectivity, the two VF cases underestimate the median by 6 to 10 dBZ_e (Fig. 13, top row). In these cases, the median of NS (nonspherical scattering) reflectivity more closely matches observations.

Conversely, for the two C-AC cases (middle row), the Mie reflectivity distribution and medians more nearly match observation than the NS distribution. For instance, the median NS reflectivity exceeds observation by over 7 dBZ_e. For the C-CM cases (bottom row), the medians of Mie and NS reflectivity encompass the observed median. In general, NS reflectivities tend to be larger than Mie reflectivities for the simulated dominance of plates and irregular polycrystals, which is consistent with a direct comparison of the scattering models for equivalent spherical volume radii less than 500 μm.

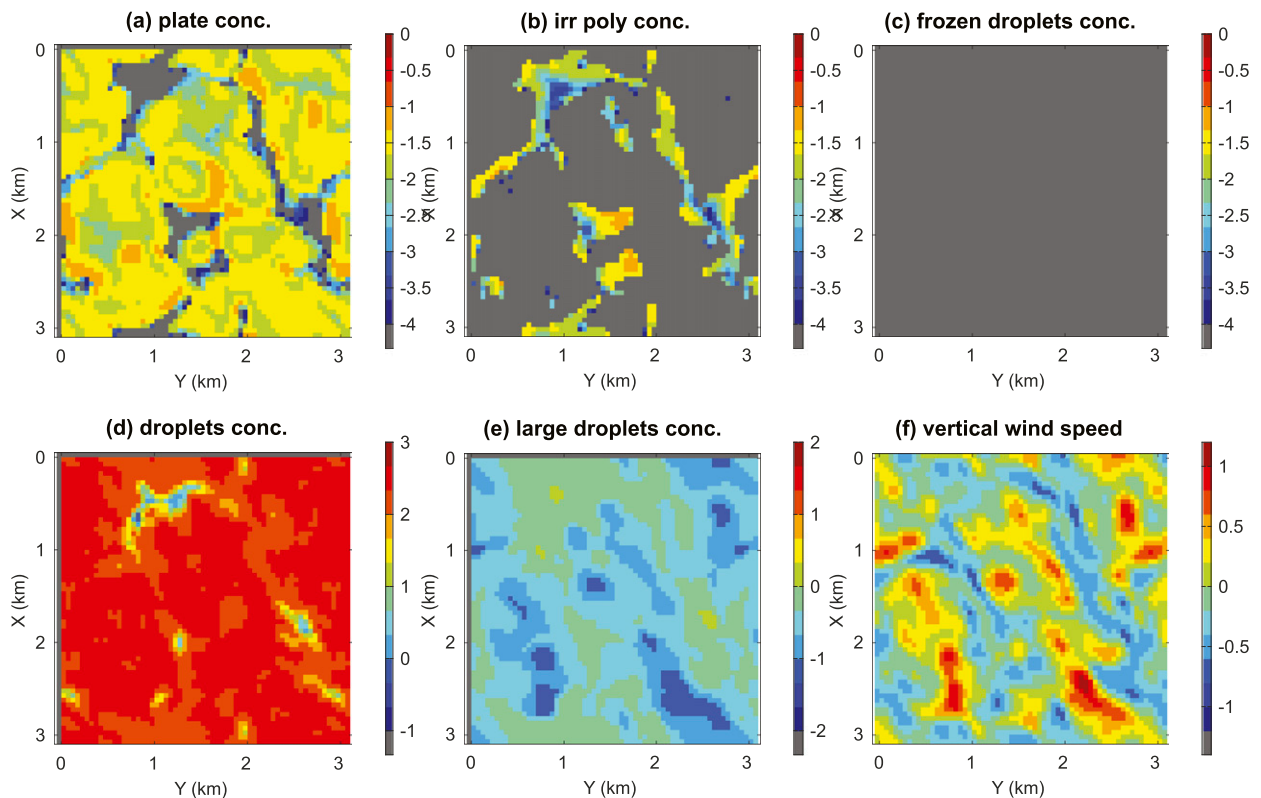


FIG. 9. As in Fig. 6, but for C-AC9.

Interestingly, the reflectivity distribution calculated with a lower freezing efficiency can be broader than that with a higher freezing efficiency. Quantitatively, the increased distribution width for VF10 over that for VF14, as defined by interquartile range (IQR), fits observations better than

the narrower distributions generated with the VF14 simulation (Table 6). The C-CM07 simulation also shows a slight increase of the width when compared with the C-CM2. But, to the contrary, the C-AC cases show an increase of the IQR with the increase in the freezing efficiency.

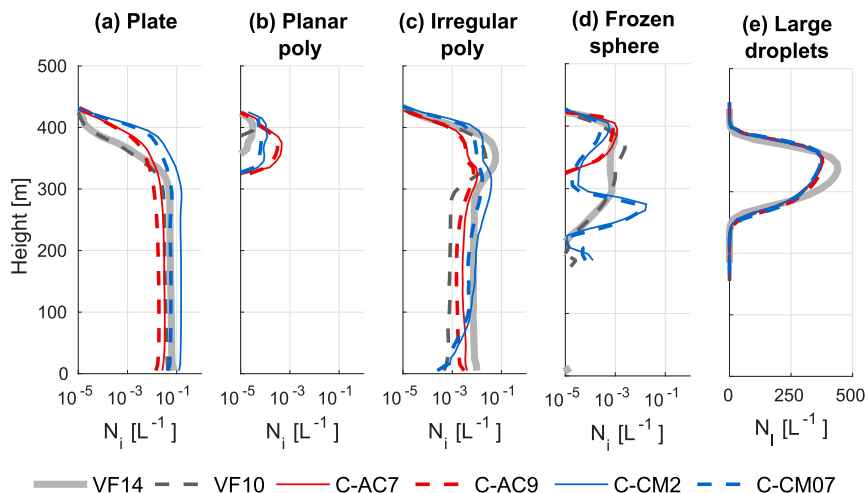


FIG. 10. Vertical profiles of average number concentration of (a) plates, (b) planar polycrystals, (c) irregular polycrystals, (d) frozen droplets, and (e) large cloud droplets for all cases. The average was calculated in the domain over the last 2 h of simulation.

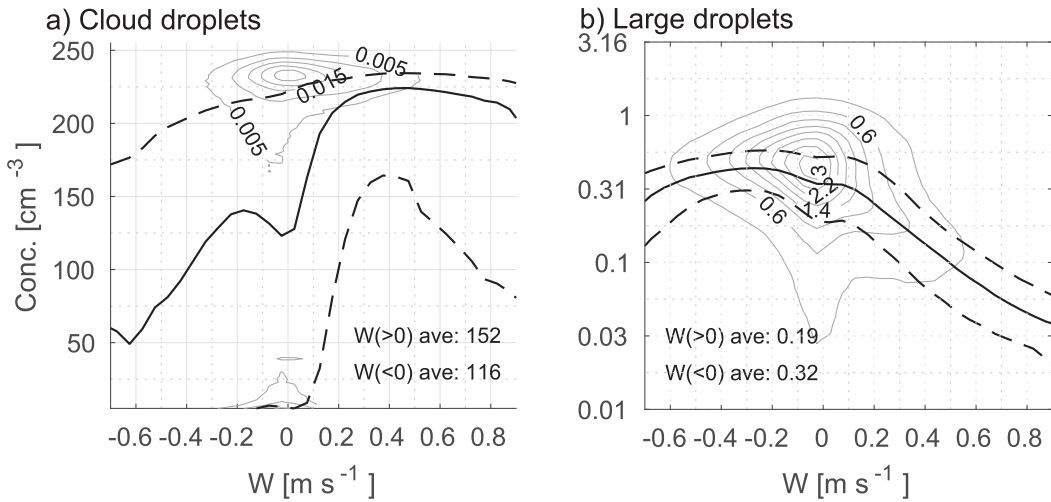


FIG. 11. Relationships between vertical motion and droplets for VF14 during the last 2 h of simulation. (a) Number concentration of cloud droplets ($1 < D < 50 \mu\text{m}$). (b) Number concentration of large droplets ($30 < D < 100 \mu\text{m}$). The lower dashed, solid, and upper dashed black curves are 25th, 50th, and 75th quantiles, respectively. The gray contours indicate joint PDFs. Samples are from grid boxes with a liquid mixing ratio $> 10^{-3} \text{ g kg}^{-1}$ in the region $250 \leq z \leq 400 \text{ m}$.

Furthermore, for each freezing scheme, the case with larger IQR indicates a larger average maximum variance of vertical velocities (Table 6). The joint PDFs of reflectivity and vertical velocity is shown in Fig. 14 for

the VF and C-AC cases. In both cases, the grid boxes with strong downdrafts tend to possess small reflectivities, the updrafts having larger reflectivity. F12 failed to reproduce observed occurrences of small

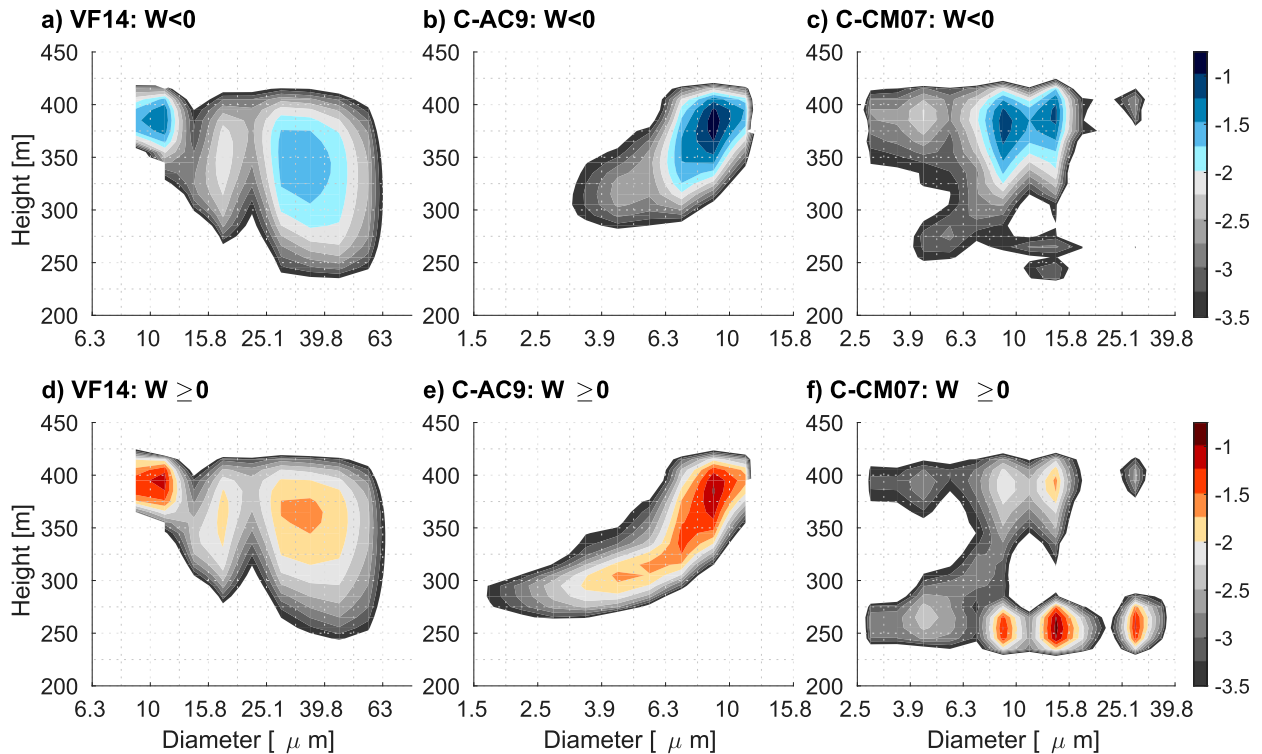


FIG. 12. Normalized freezing rates in terms of droplet diameter and height over the last 2 h of simulation of the three nucleation schemes in (a)–(c) downdraft regions and (d)–(f) updraft regions. The unit is $\log_{10}[1/\text{m}/\log_{10}(\mu\text{m})]$.

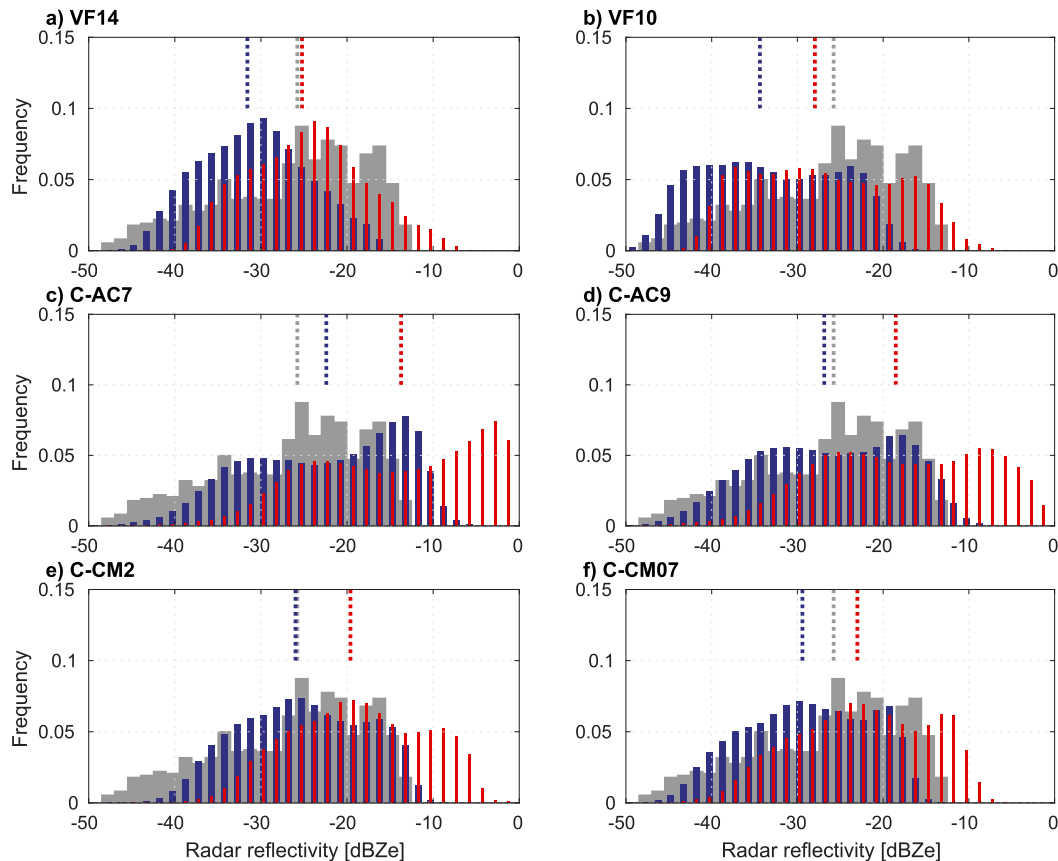


FIG. 13. Radar reflectivity histograms during the last hour of simulation for all cases. (a) VF14. (b) VF10. (c) C-AC7. (d) C-AC9. (e) C-CM2. (f) C-CM07. Samples were taken below the cloud base ($82.5 < z < 217.5$ m). The gray bars indicate observation of MMCR during 2200 to 2400 UTC. Dark blue bars are from the Mie approximation; red bars are from the nonspherical scattering database. Medians are marked by dotted vertical lines from the top.

reflectivity that were associated with alternating period of increases and decreases in reflectivity, and inferred that the time scale of alternation was related to the mesoscale horizontal variability. We have shown here that the parameters related to the ice nucleation process can be a controlling factor in the production of wider distributions of radar reflectivity.

e. Comparison of particle size distributions and aspect ratios

Ice particle size distributions averaged in space and time below the cloud show characteristics that stem from

the ice nucleation schemes. Figure 15a shows particle size distributions for ice averaged during the last hour of simulation between 82.5 and 217.5 m, corresponding to the altitude range in the radar reflectivity histograms. The C-AC cases produce bimodal distributions with modes at 70 and 500 μm , while the VF and C-CM cases produce unimodal distributions, with a peak at 300 μm .

Figure 15b shows the median axis ratio of hexagonal plates for a given maximum dimension D_{mx} . The axis ratio is defined as the c -axis length over a -axis length. The C-AC cases predict axis ratios between 0.04 and

TABLE 6. IQR of radar reflectivity below the cloud layer ($82.5 < z < 217.5$ m) during the last hour. IQR is defined as the 75th percentile minus the 25th percentile. Average maximum variance of w ($W_{\text{var,max}}$) is calculated as follows. First, a profile of variance of vertical motions was calculated every 150 s at $z < 600$ m, and then the maximum value was averaged over the last hour.

	VF14	VF10	C-AC7	C-AC9	C-CM2	C-CM07	OBS	No-CRS	No-CLL	Diag-PL
IQR for Mie	9.2	13.3	15.0	13.9	11.5	11.6	13.1	11.3	9.4	17.8
IQR for NS	9.6	14.3	17.1	16.0	12.0	12.2	13.1	11.4	10.0	19.9
$W_{\text{var,max}}$	0.16	0.27	0.27	0.24	0.24	0.27	—	0.21	0.16	0.26

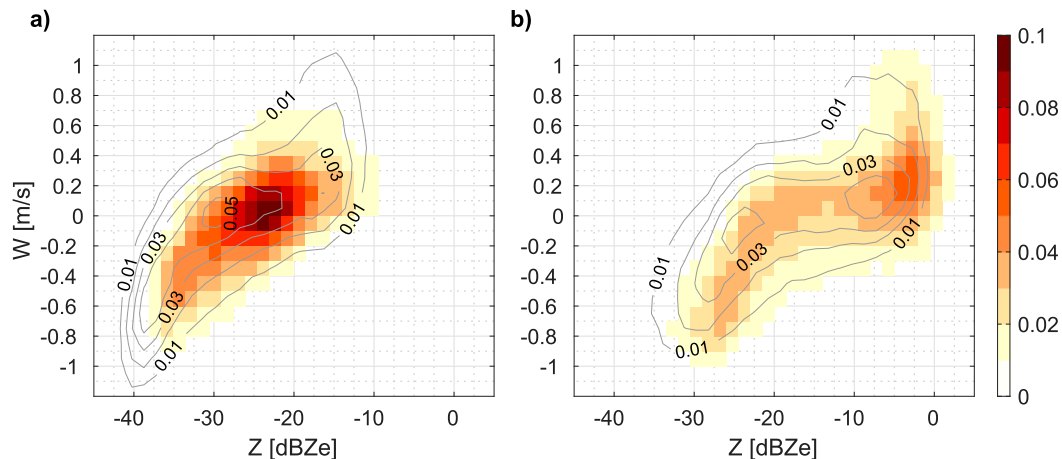


FIG. 14. Joint PDFs of vertical velocity and radar reflectivity during the last hour of simulation for VF and C-AC schemes. Samples are from below the cloud base ($82.5 < z < 217.5$ m). (a) VF14 (color fill) and VF10 (contours). (b) C-AC7 (color fill) and C-AC9 (contours).

0.08 with the ratio being smaller for larger D_{mx} . On the other hand, the axis ratio simulated by VF and C-CM cases are nearly one order of magnitude larger, varying between 0.1 and 0.7. Comparison of VF14 and VF10 indicates that the predicted axis ratios depend on the ice nucleation parameters, with less efficient cases tending to simulate larger axis ratios.

To investigate a relationship between droplet sizes at the time of freezing and plate growth, average axis ratios predicted for a given D_{mx} of hexagonal plates and the

diameter at freezing D_{frz} inside the ice crystal were calculated for VF14, C-AC9, and C-CM07 below the cloud layer (Fig. 16); D_{frz} is the diameter of the ice sphere whose mass is the frozen nucleation mass component of a particle (see appendix A). For instance, in the C-AC9 case (Fig. 16b), at a constant D_{mx} between 316 and 3162 μm , the average axis ratio decreases as D_{frz} inside the ice particle decreases. Qualitatively similar axis ratio trends are observed for VF14 and C-CM07. This relation between the crystal initial size and axis

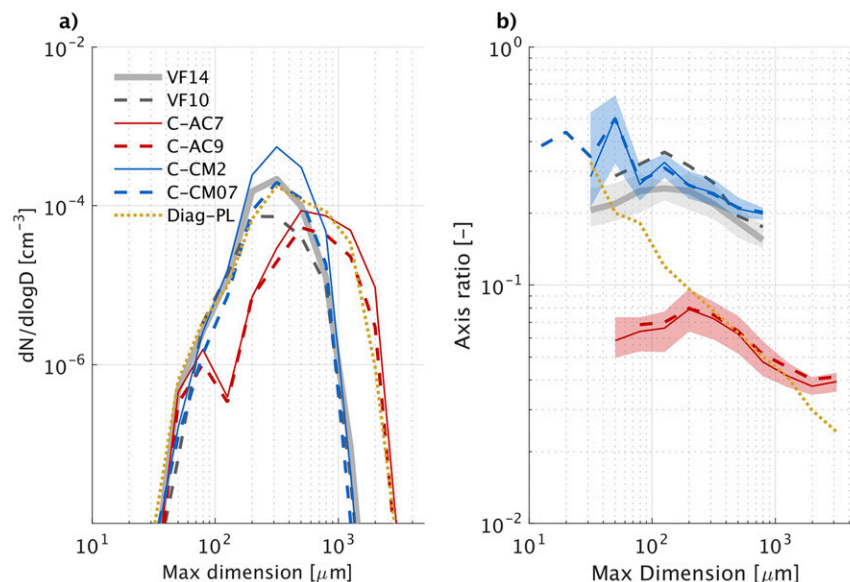


FIG. 15. Hexagonal plate distributions for all cases. (a) Average particle size distribution. (b) Median axis ratio. Shades in (b) indicate the range between the 5th and 95th percentiles for VF14, C-AC7, and C-CM2. The averages and percentiles were calculated between 82.5 and 217.5 m in the domain over the last hour of simulation.

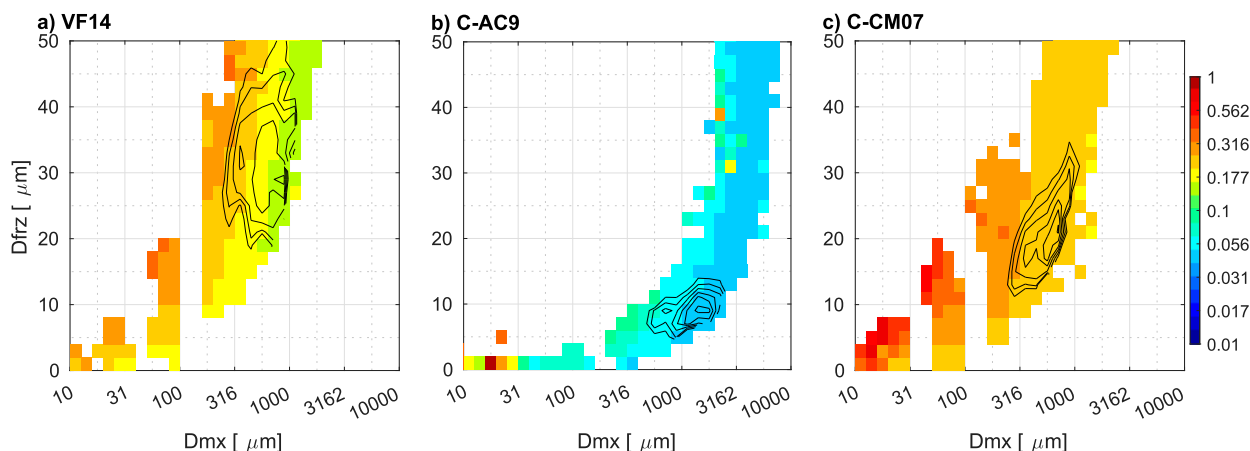


FIG. 16. Average axis ratio (color fill) in the space of maximum dimension of ice particle (D_{mx}) and diameter of freezing droplet inside of ice particle (D_{frz}). (a) VF14. (b) C-AC9. (c) C-CM07. The black contours are the joint PDF weighted by radar reflectivity in units of $\log_{10}[1/\log_{10}(\mu\text{m})/\mu\text{m}]$. Samples come from between 82.5 and 217.5 m.

ratio has been explained analytically by [Sulia and Harrington \(2011\)](#). That is, a smaller initial mass leads to more extreme axis ratios and larger mass through a nonlinear positive-growth feedback built into the habit prediction scheme by [Chen and Lamb \(1994\)](#). However, the axis ratios for a pair of D_{frz} and D_{mx} are not the same among the cases, suggesting hysteresis of vapor-depositional growth related to temperature and supersaturation experienced by the hexagonal plates that is not explained solely by D_{frz} .

The frozen nucleation mass introduced in this study (and D_{frz} diagnosed from it) is a useful tracer to infer the location of freezing. Joint PDFs weighted by radar reflectivity below the cloud layer are shown as black contours in [Fig. 16](#). In the case of VF14, it is clear that the radar reflectivity can be attributed to hexagonal plates with $D_{mx} \sim 560 \mu\text{m}$ that were nucleated from large cloud droplets with $D \sim 30 \mu\text{m}$, whereas the freezing of $D \sim 10\text{-}\mu\text{m}$ droplets close to the cloud top ([Fig. 12a](#)) does not contribute to the radar reflectivity distribution. On the other hand, in C-AC9 hexagonal plates that initiated near the cloud top from $D \sim 10\text{-}\mu\text{m}$ cloud droplets ([Fig. 12b](#)) are responsible for the radar reflectivity. For C-CM07, the hexagonal plates with $D_{mx} \sim 560 \mu\text{m}$ contribute to the below-cloud radar reflectivity the most, and these have $D_{frz} \sim 18 \mu\text{m}$. According to [Fig. 12c](#), the droplet freezing modes closest to this diameter are near the cloud base in the region of updrafts.

In conclusion, the simulations suggest that the PSDs in the well-mixed layer are characterized by the initial size of the ice crystals upon freezing from cloud droplets. The axis ratio of hexagonal plates in this region depends in part on the initial size at ice crystal nucleation, and

thereby is influenced directly by the ice nucleation scheme.

4. Discussion

a. Fixing mass–dimensional relationship of plates

Averaged over a domain, the simulated axis ratio of hexagonal plates converges to values that are partly determined by the ice nucleation scheme ([Fig. 15b](#)). Here we discuss the effects of prescribing a mass–dimensional relationship of plates with the Diag-PL case ([Table 3](#)).

For Diag-PL, the domain-average time series of LWP and N_i are nearly the same as those for VF14, but the IWP is almost twice as large ([Fig. 1](#)). The histogram of radar reflectivity calculated for Diag-PL ([Fig. 17a](#)) differs from that of VF14, with the median of reflectivity derived using the Mie calculation being similar to the observed one and the spread being larger than that for VF14. Corresponding to the two modes evident in the reflectivity distribution, the maximum variance of vertical velocities is comparable to those in VF10, C-AC7, and C-CM07 ([Table 6](#)). This case clearly indicates that the habit affects the vertical velocity and turbulence. The average N_d is actually larger than that in VF14 ([Fig. 1c](#)), suggesting that the strengthened updraft increases the supersaturation and thus leads to additional cloud droplets. The reason for the larger vertical velocities could be related to the smaller axis ratio than that in VF14 ([Fig. 15b](#)), resulting in a larger capacitance, slower sedimentation, and wider particle size distribution ([Fig. 15a](#)). These changes in turn could increase the latent heat release, invigorating the updrafts. Such a result contrasts with a previous assumption that

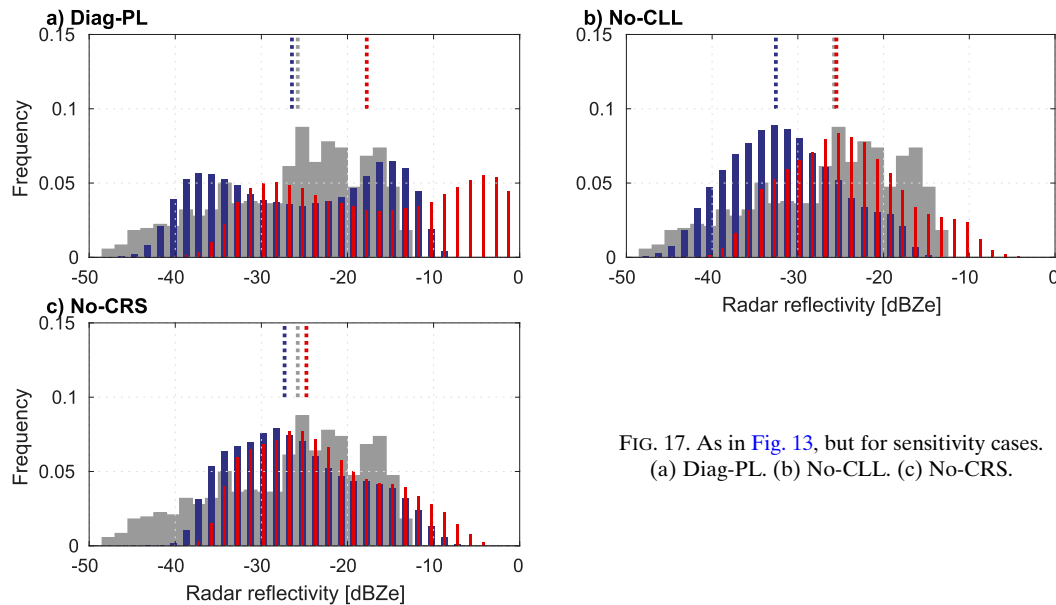


FIG. 17. As in Fig. 13, but for sensitivity cases. (a) Diag-PL. (b) No-CLL. (c) No-CRS.

the use of thin plates for the cloud ice shortens the lifetime of mixed-phase clouds compared to that when using ice spheres. More importantly, use of fixed mass-dimensional relationships may not simulate nonlinear feedbacks properly even if the size of freezing droplets is taken into account.

b. What produces the large droplets?

Given the importance of the large drops in the freezing process, we seek to clarify the origin of these droplets ($D > 30 \mu\text{m}$) with the No-CLL and No-CRS cases (Table 3). Note that the average vertical profiles of $N_{c,\text{large}}$ are actually similar among the cases (Fig. 10e).

The radar reflectivity distribution from No-CLL (Fig. 17b) is almost identical to that in VF14 (Fig. 13a), meaning that the collision-coalescence process appears to have minimal impact on the ice crystals below the cloud layer. We also found that the vertical profile of number concentration of large droplets $N_{c,\text{large}}$ was similar to VF14 although it is slightly reduced at the peak (Fig. 18e). The same is true for the habit distribution (Fig. 18). On the other hand, in the No-CRS simulation $N_{c,\text{large}}$ is negligible (Fig. 18e). The results of these cases indicate that large droplets are the result of including the coarse mode in the wet transfer scheme.

Due to the lack of ice nucleation associated with large droplets at $T > -20^\circ\text{C}$, the No-CRS case simulated a dominance of irregular polycrystals (Fig. 18c). The dominance of polycrystals is consistent with F12's qualitative assessment of habit frequency with CPI

images that plates were minor. The differences in crystal habit that stem from a lack of large droplets appear on the radar reflectivity distribution (Figs. 13a and 17c). Furthermore, the differences between Mie and nonspherical scattering calculations in the reflectivity distribution are relatively small for the No-CRS simulation (Fig. 17c), which corresponds to the abundance of irregular polycrystals (Fig. 18c). As the ice scattering model assigned to irregular polycrystals is that for bullet rosettes whose bulk density is relatively high, the difference in backscatter coefficient from the Mie calculation was smaller than that for the other crystals with an equivalent spherical volume radii less than $500 \mu\text{m}$. In situ measurements of spatial habit distribution are necessary to further evaluate the impacts of coarse-mode aerosol particles.

c. How realistic is it to have large droplets freezing?

We consider several indications that large droplets in these clouds freeze. For example, the measured particle-size distribution in the cloud layer has a smaller mode around $10 \mu\text{m}$ and a larger mode around $40 \mu\text{m}$ (see F12, their Fig. 3). The larger mode suggests the existence of large droplets that could contribute to ice nucleation. Other studies have reported the coexistence of such large drops ($>30 \mu\text{m}$) with ice particles in cases of active ice precipitation (e.g., Lance et al. 2011). The VF and C-CM cases here indeed freeze the large droplets that then develop into plates of relatively large axis ratio.

To examine the state of activation, consider the droplet size distribution in the cloud layer together with critical radius of CCN activation R_{cr} . Figure 19a shows

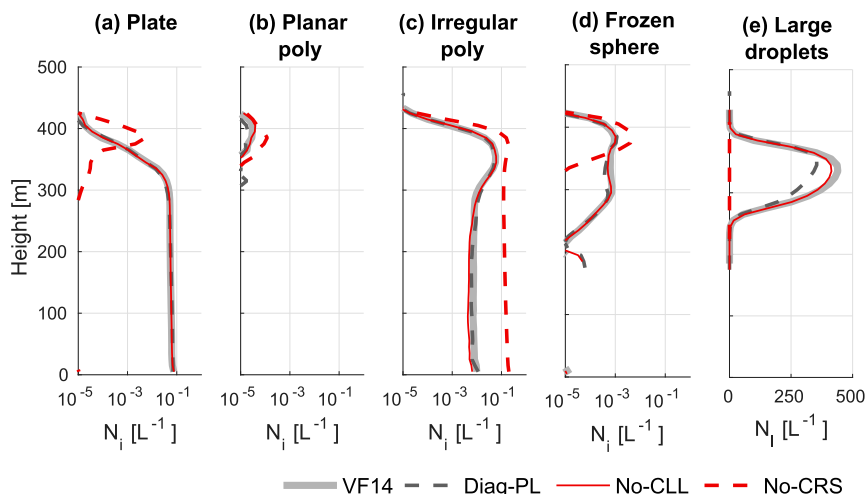


FIG. 18. As in Fig. 10, but for sensitivity cases of Diag-PL, No-CLL, and No-CRS. VF14 is shown as a reference.

the joint PDF (black contours) of droplet diameter D and R_{cr} together with the normalized freezing rate (colored rectangles) obtained for VF14 during the last 2 h of simulation. As the thick solid line indicates $R_{cr} = D/2$, the samples above the line are in the unactivated state. The observed mode of cloud droplets around $10\ \mu\text{m}$ was simulated, with most droplets activated. However, additional modes around 1, 18, and $32\ \mu\text{m}$ fall above the activation line, and have therefore not been activated in the model. Nevertheless, these unactivated droplets (haze droplets) can freeze in the VF14 scheme, and significantly contribute to the freezing nucleation (as indicated by the color fill).

Concerning the other cases, for No-CRS, mainly the droplets of about $10\ \mu\text{m}$ that have been activated freeze (Fig. 19b) because the coarse mode particles have been ignored. The C-AC9 case shows three modes in the liquid spectrum (Fig. 19c), like that in VF14 (Fig. 19a), yet has a different freezing rate. However, because the C-AC scheme allows the CNT immersion freezing parameterization to act only for activated droplets, none of the unactivated droplets can freeze, making the freezing rate distribution looks markedly different than that of the VF14 case. But the C-CM scheme allows the freezing of coarse mode aerosol particles, and thus most of the droplets that freeze are related to droplets in an unactivated state (Fig. 19d). The activated droplets are not freezing due to the assumption that the INP inside the droplet must exceed $0.5\ \mu\text{m}$. The resulting freezing pattern for C-CM is similar to that from VF, but the high freezing rate is shifted to a slightly larger R_{cr} .

The freezing rate of large droplets in the C-CM schemes is controlled by the size of the INPs, but the effect is modified by the minimum contact angle in the

quasi-steady state. Weighted averages of D_{INP} , θ_{00} , and molality were calculated with the freezing rate of droplets being weights as indicated with color fills (Fig. 20). The top row is for downdraft regions; the bottom row is for updraft regions. For both downdrafts and updrafts, the D_{INP} average increases monotonically with D at fixed height for most heights (left column). Similarly, the θ_{00} average increases with D at a given height, but is limited to the specified upper bound of 100° (center column).

The molality averages (right column) differ somewhat from the other two variables. Molality typically decreases where condensation occurs, whereas D_{INP} stays constant. For instance, in the updrafts, the molality decreases from about 0.8 at $D = 3\ \mu\text{m}$ and $z = 250\text{ m}$ to 0.015 at $D = 10\ \mu\text{m}$ and $z = 355\text{ m}$, whereas D_{INP} stays in the range of $0.6\text{--}0.64\ \mu\text{m}$. The freezing probability for a INP-containing droplet was calculated by dividing the freezing rate with the total number of dust particles included in liquid mass bins, $\sum_b N_{l,inp}^b$ (see white contours in Fig. 20). For instance, large droplets of $D = 35.5\ \mu\text{m}$ at 255 m with $D_{INP} = 12.1\ \mu\text{m}$, $\theta_{00} = 99.6^\circ$, and molality = 5.2 likely freeze in updrafts. Comparison to the average D_{INP} and freezing probability indicates that the probability increases monotonically with D_{INP} . However, the probability starts to decrease beyond about $D_{INP} = 32\ \mu\text{m}$. The decrease occurs because θ_{00} takes on values exceeding 90° on average, which is close to the upper limit of the contact angle for freezing ($\theta_{00} = 100$). In the quasi-steady state during the last 2 h of simulation, the low freezing probability is related to low θ_{00} . Furthermore, the molality plays a minor role on the freezing in the C-CM scheme. The weighted-average molality calculated over height and diameter is 5.4 (2.2) in updrafts (downdrafts) (shown inside of Figs. 20c,f).

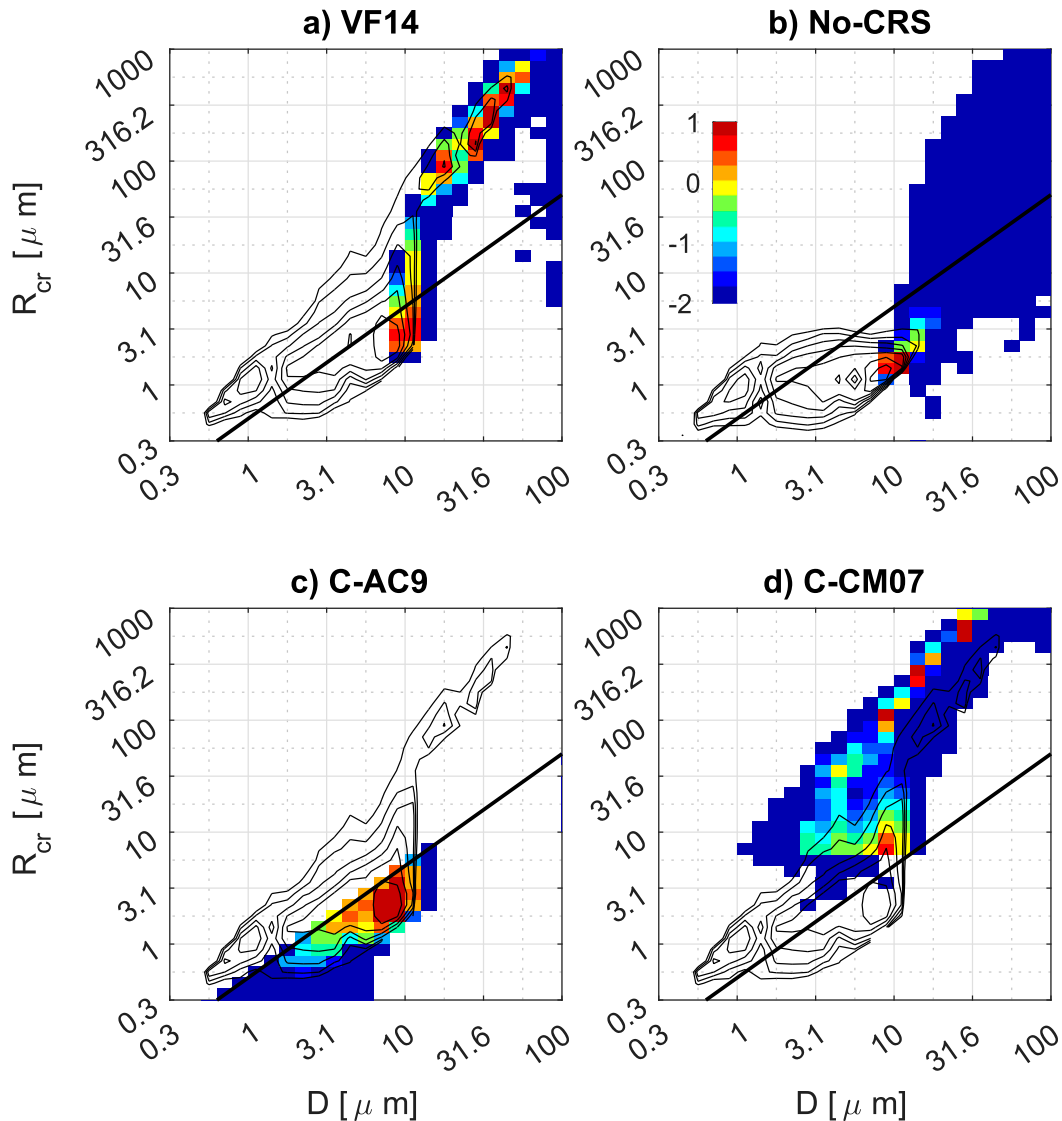


FIG. 19. Normalized freezing rate (color fill) in the space of cloud-droplet diameter and critical radius of activation during the last 2 h of simulation. (a) VF14. (b) No-CRS. (c) C-AC9. (d) C-CM07. Samples are from $220 < z < 400$ m. The thick solid line is $D = 2R_{cr}$. The units are $\log_{10}[1/\log_{10}(\mu\text{m})/\log_{10}(\mu\text{m})]$. Joint PDFs of the droplet diameter and critical radius are overlaid with solid contours at -2 to $1 \mu\text{m}$ in equal increments of $0.5 \mu\text{m}$.

These are quite large compared to a rough limit (0.001) for freezing temperature depression to occur (Pruppacher and Klett 1997, p. 354).

The active freezing at the cloud base in updrafts and at the cloud top in downdrafts is explained by advection of fresh aerosol particles from subsaturated to water-saturated regions.

We examine in Fig. 21 the joint PDFs of z and D with dust concentrations within liquid droplets (left column) together with the freezing probabilities (right column). The area enclosed by the -3 contour depicts the feature of condensational growth. In updraft regions, transfer of the aerosol particles into the small liquid bins ($D < 1 \mu\text{m}$)

mostly occurs near cloud base and cloud top (Fig. 21d). On the other hand, the wet transfer in downdraft regions mainly occurs near cloud top (Fig. 21b). For both updraft and downdraft regions, there is a direct contribution of wet transfer to the concentration of large (haze) droplets ($> 10 \mu\text{m}$). As a result, near the cloud base and top, the D_{INP} are a few factors smaller than D (Figs. 20a,d).

5. Conclusions

To investigate how different ice nucleation schemes affect simulated ice crystal habits, we ran a series of 3D LES experiments using the UW-NMS AMPS. The cloud case

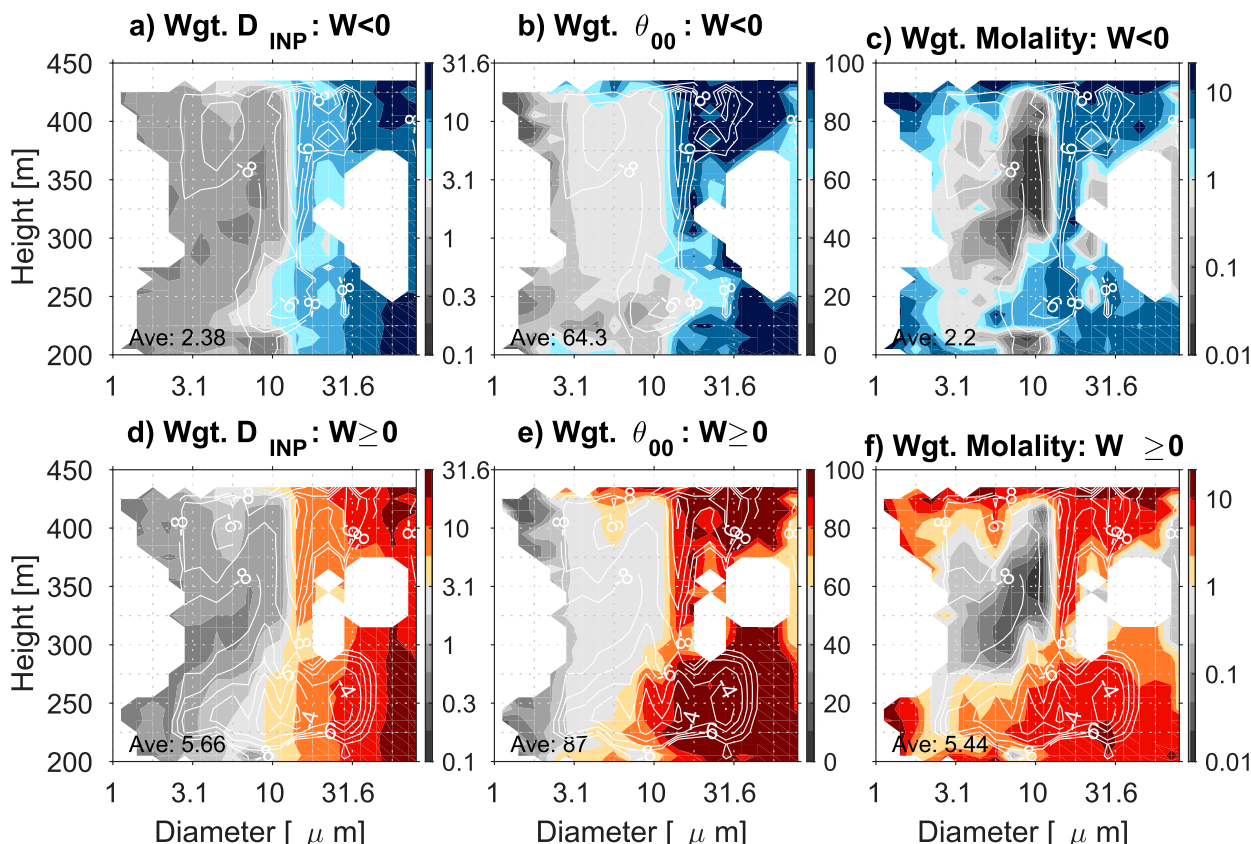


FIG. 20. Weighted-average INP parameters within liquid particles for C-CM07 calculated during the last 2 h in (a)–(c) downdraft regions and (d)–(f) updraft regions. (left) Diameter D_{INP} (μm). (center) Weighted-average θ_{00} ($^{\circ}$). (right) Weighted-average molality (mol kg^{-1}). Freezing probability per INP-containing droplet [$\log_{10}(\text{s}^{-1})$] is indicated with white contours. Numbers next to “Ave” are the weighted-average values calculated over height and diameter.

chosen for these simulations was a mixed-phase stratiform cloud observed during the SHEBA campaign on 7 May 1998. To the predicted habit distributions, we applied a satellite data simulator (Joint-Simulator) to simulate the resulting radar reflectivities from the different ice nucleation schemes. Three immersion-freezing parameterizations were tested: a volume-dependent freezing scheme (VF), an activated-droplet scheme (C-AC), and a coarse-mode scheme (C-CM), with the latter two schemes being based on a parameterization of classical nucleation theory (CNT). Over the 4-h simulation, all of these simulations maintained a domain-averaged LWP corresponding to the range observed, but they produced distinct relationships between the averaged droplet and ice concentrations.

The three immersion freezing schemes produced different in-cloud freezing locations and different sizes of freezing droplets. With the VF scheme, a relatively large number of small droplets froze near the cloud top because the low-temperature influence offset their small volume, whereas the large droplets tended to freeze throughout the cloud due to the volume effect. In addition, large cloud

droplets of about $30\text{-}\mu\text{m}$ diameter tended to freeze near and in downdrafts. The C-AC scheme requires the droplets to be both activated and to have a sufficiently low temperature. As a result, most freezing occurred near the cloud top where it involved droplet diameters of about $8\text{-}\mu\text{m}$ and high supersaturations in an updraft region. For the C-CM scheme, the INP diameter and the lower threshold of contact angles control the freezing rate in addition to the temperature and the presence of INPs. However, in this case, high molality did not prevent droplets from freezing. As a result, the locations of freezing were related to the wet transfer process. Droplets with $8\text{--}32\text{-}\mu\text{m}$ diameters were shown to freeze near the cloud base and contribute significantly to the total freezing rate.

These different immersion freezing schemes shared the following characteristics of habit distribution:

- The 3D habit distribution generally indicated dominance of irregular polycrystals near cloud top, whereas plates prevailed below the lower half of the mixed-phase cloud layer.

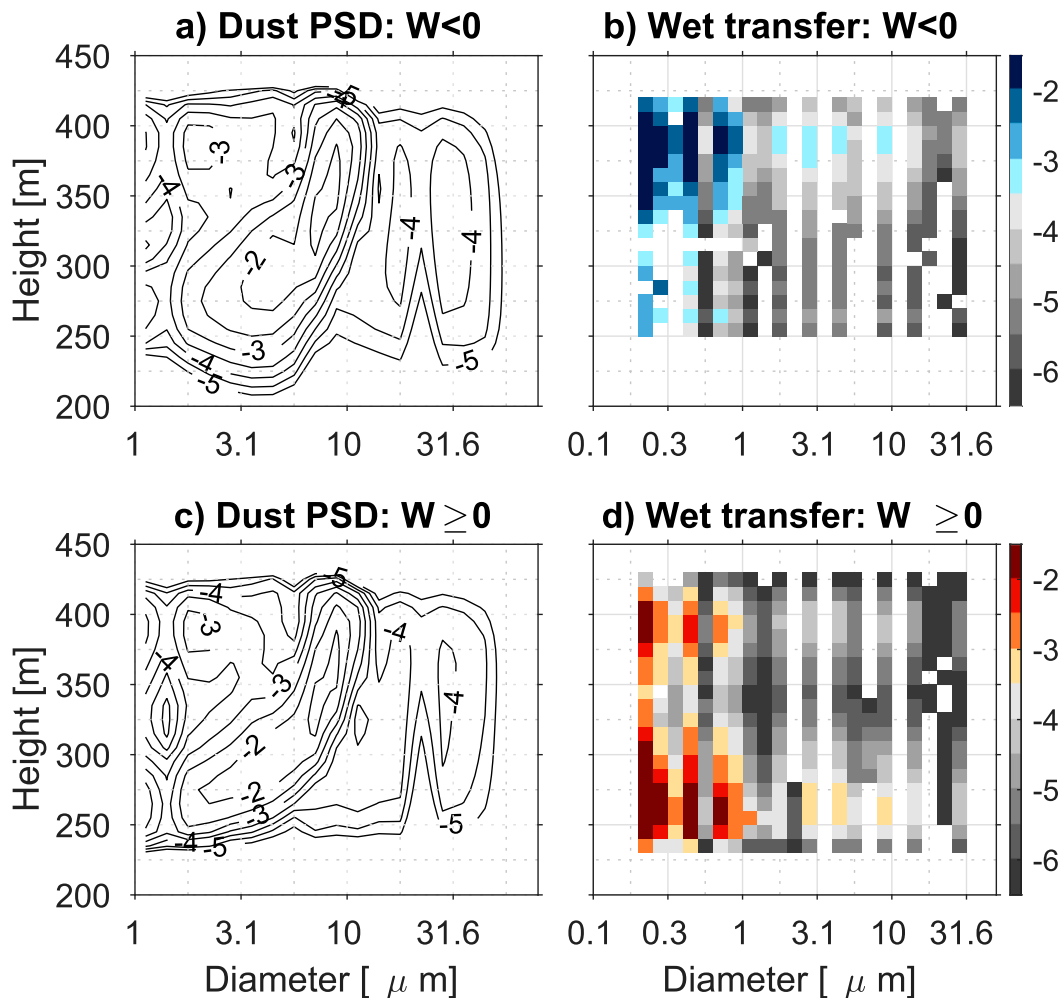


FIG. 21. Joint PDFs of dust particles within the droplets and normalized wet transfer rate for C-CM07 calculated during the last 2 h in (a),(b) downdraft regions and (c),(d) updraft regions. The joint PDFs and wet transfer rates are both in $\log_{10}[1/\log_{10}(\mu\text{m})/\text{m}]$.

- The irregular polycrystals appeared in a band-like structure associated with downdrafts and the plates appeared with a cell-like distribution related to updrafts.
- Frozen spheres would occur where the freezing rates were high, which varied by the freezing scheme.

This habit distribution agrees qualitatively with observations by [Korolev et al. \(2000\)](#) in ice-only stratiform clouds. However, our study is the first to show such spatial distribution numerically. The irregular polycrystals are the results of applying a frequency diagram ([Bailey and Hallet 2004](#)) at temperatures below -20°C , and their common occurrence highlights the importance of characterizing their growth parameters and fall velocity for realistic simulation of mixed-phase clouds.

We demonstrated theoretical links between crystal habits and immersion freezing processes. Differences

in the initial size of freezing droplets were linked to differences in the simulated axis ratios of hexagonal plates (up to one order of magnitude difference), owing to the [Chen and Lamb \(1994\)](#) parameterization. These differences are reflected in the particle size distribution and histogram of radar reflectivity below the cloud layer. The finding suggests that it might be possible to identify the size of droplets freezing or mode of freezing from remote sensing observations that are sensitive to aspect ratio of particles, methods such as lidars and multiparameter radars. However, it is critical to test the links with physical laboratory settings as well as with in situ observations. Also, the vertical distribution of habits was significantly affected by the selection of immersion freezing scheme and the assumed aerosol size distribution. We emphasized that cloud microphysical schemes with

habit-prediction capability are an important tool to properly investigate the relationships among ice nucleation processes, crystal habit, and dynamics. Nevertheless, it is important to further validate and improve habit-predicting schemes. As the habit-predicting bulk schemes (Harrington et al. 2013; Chen and Tsai 2016; Jensen et al. 2017) fix the initial size of crystals, the above link is not simulated. We are presently exploiting Doppler velocity spectra to validate the scheme and identify signatures of immersion freezing, and will report in a future paper.

In all cases, large haze droplets occurred more in downdraft regions than in updraft regions. The droplet number concentrations were found to converge over downdraft regions, which contributes to maintaining the droplet number concentration in a quasi-steady state against the loss due to the freezing process. It is also expected that the rate of condensation is not fast enough for the droplets to grow to large sizes in updraft regions. These could be a common feature of such shallow stratiform clouds.

The unactivated large droplets were shown to contribute significantly to immersion freezing. The VF scheme produced a freezing dependence on droplet diameter and activation radius similar to C-CM, a CNT scheme. Therefore, the VF scheme is still a reasonable choice when subgrid-scale motions and aerosol particles are not reliable or available. The C-CM scheme with dust fractions typical for a clean environment and with contact angle characteristics derived from a set of physical laboratory experiments produced the LWP and IWP in the observed range as well as the radar reflectivity distribution. In this sense, it is a promising scheme for such clouds. Further work should be done to improve representation of the INP size distribution within a single droplet in a model and to understand evolution of the surface area of INPs within liquid droplets in real clouds in addition to the material type.

Acknowledgments. This research was supported by the Japan Society for the Promotion of Science Grant-in-Aid for Young Scientists (B) Grant JP16K17803 and Arctic Challenge for Sustainability project (ArCS). G. de Boer was supported by the U.S. Department of Energy (DOE) Atmospheric System Research (ASR) program under Project DE-SC0013306. H. Okamoto was supported by Japan Society for the Promotion of Science Grant-in-Aid for Scientific Research (S) Grant JP17H06139 and ArCS. The computation was mainly carried out using the computer facilities at Research Institute for Information Technology, Kyushu University. The authors are grateful to the anonymous reviewers for their valuable and constructive comments.

APPENDIX A

Diagnosis of Frozen Spheres

In the immersion freezing parameterizations, the frozen mass of a given ice bin is incremented through transfer of mass from a liquid mass bin to the ice particle spectrum. The frozen mass serves as a tracer of the freezing process, and the mass can be used to diagnose the conceptual shape of an ice particle with a certain amount of the frozen mass as a sphere. That is, “sphere” is introduced as an ice particle model in addition to “cylinder” and “spheroid” (see Hashino and Tripoli 2011a) because quasi-spherical particles are often observed in clouds (e.g., Korolev et al. 2004; Bailey and Hallet 2009). As spherical crystals fall faster and have a lower capacitance than nonspherical particles for the same volume, ice particle shapes have an important influence on the simulated lifetime of mixed-phase clouds (Sulia and Harrington 2011).

We use two criteria to diagnose the particles in a given mass bin as ice spheres. One, if the frozen nucleation mass component of a particle m_{IF} is more than the mass of an ice sphere with 100- μm diameter. Two, if the following is satisfied by the total ice crystal mass m_I :

$$F_s m_{\text{IF}} > m_I, \quad (\text{A1})$$

where the factor F_s is set to 8 for this study. Consider that a spherical frozen particle is contained in a larger ice sphere. The $F_s = 8$ condition corresponds to having the diameter of the spherical frozen particle (“IF” subscript) being more than half of that of the larger ice sphere (“I” subscript). These mass components generally satisfy the relationship $m_I = m_{\text{IF}} + m_{\text{VD}}$, where m_{VD} denotes the mass due to vapor deposition. The first criteria is based on a laboratory experiment with use of a thermal diffusion chamber (Korolev et al. 2004). The second condition is somewhat subjectively determined. Gonda and Yamazaki (1984) showed that a frozen droplet of diameter around 20 μm quickly transformed into eight-faced crystal of diameter 26 μm , which gives $F_s = 2.7$. Given this limited information on the mass or size threshold for small droplets, the $F_s = 8$ is a simple and reasonable choice.

APPENDIX B

Formulas Used in the Parameterization Based on Classical Nucleation Theory

Chen et al. (2008) gives the preexponential factor A_{imm} as

$$A_{\text{imm}} = 2 \frac{kT}{h} c_{1,s} \frac{v_i}{r_{\text{cr}}^2} \sqrt{\frac{\sigma_{i/s}}{kT}} \sqrt{f(\theta)}, \quad (\text{B1})$$

where $c_{1,s}$ is the concentration of water monomers adsorbed on the ice/nucleus surface, v_i is the molar volume of ice, r_{cr} is the critical radius of an ice germ, $\sigma_{i/s}$ is the surface tension between the ice–solution interface, h is the Planck’s constant, and $f(\theta)$ is a geometric factor. $\sigma_{i/s}$ is the absolute difference of surface tensions between solution–vapor and ice–vapor, where the former is calculated with

$$\Delta G_{\text{act,imm}} = \begin{cases} 0.694 \times 10^{-12} [1 + 0.027(T_c + 30)] & \text{for } T_c > -30^\circ\text{C} \\ 0.694 \times 10^{-12} [1 + 0.027(T_c + 30)] \exp[0.01(T_c + 30)] & \text{for } T_c \leq -30^\circ\text{C} \end{cases}, \quad (\text{B2})$$

where T_c is the air temperature in Celsius. Here, $\Delta G_{g,\text{imm}}$ is calculated as

$$\Delta G_{g,\text{imm}} = \frac{4\pi \sigma_{i/s} r_{\text{cr}}^2}{3 kT}, \quad (\text{B3})$$

and r_{cr} is calculated as

$$r_{\text{cr}} = \frac{2\sigma_{i/s}}{\rho_i L_m^{\text{ef}} \left[\ln\left(\frac{T_0}{T}\right) + G_n \ln(1 + s_w) - H_{v,\text{fr}} \right]}, \quad (\text{B4})$$

where ρ_i is the ice density, s_w is the vapor supersaturation over liquid water, L_m^{ef} is the effective specific melting heat averaged over the temperature [Eq. (8.8.12b) of KC14], and G_n and $H_{v,\text{fr}}$ are the nondimensional parameters [Eqs. (8.6.15) and (8.6.16) of KC14].

REFERENCES

- Auer, A. H., and D. L. Veal, 1970: The dimension of ice crystals in natural clouds. *J. Atmos. Sci.*, **27**, 919–926, [https://doi.org/10.1175/1520-0469\(1970\)027<0919:TDOICI>2.0.CO;2](https://doi.org/10.1175/1520-0469(1970)027<0919:TDOICI>2.0.CO;2).
- Avramov, A., and J. Y. Harrington, 2010: Influence of parameterized ice habit on simulated mixed phase Arctic clouds. *J. Geophys. Res.*, **115**, D03205, <https://doi.org/10.1029/2009JD012108>.
- Bailey, M. P., and J. Hallet, 2004: Growth rates and habits of ice crystals between -20° and -70°C . *J. Atmos. Sci.*, **61**, 514–544, [https://doi.org/10.1175/1520-0469\(2004\)061<0514:GRAHOI>2.0.CO;2](https://doi.org/10.1175/1520-0469(2004)061<0514:GRAHOI>2.0.CO;2).
- , and —, 2009: A comprehensive habit diagram for atmospheric ice crystals: Confirmation from the laboratory, AIRS II, and other field studies. *J. Atmos. Sci.*, **66**, 2888–2899, <https://doi.org/10.1175/2009JAS2883.1>.
- Bergeron, T., 1935: On the physics of clouds and precipitation. *Proc. Fifth General Assembly, International Union of Geodesy and Geophysics*, 156–180.
- Bigg, E. K., 1953: The formation of atmospheric ice crystals by the freezing of droplets. *Quart. J. Roy. Meteor. Soc.*, **79**, 510–519, <https://doi.org/10.1002/qj.49707934207>.
- Eq. (A13) and Table A1 of Chen (1994) for ammonium sulfate, and the latter is calculated with an equation in Table A1 of Hoose and Mohler (2012). Molality is included through the solution/vapor surface tension. The value of $f(\theta)$ is calculated with Eqs. (9)–(18) of Pruppacher and Klett (1997) for a spherical cap embryo on a planar surface as a function of contact angle θ between ice and substrate. $\Delta G_{\text{act,imm}}$ is calculated with Eqs. (8.3.23a) and (8.3.23b) of Khvorostyanov and Curry (2014, hereafter KC14):
- Borys, R., D. H. Lowenthal, S. A. Cohn, and W. O. J. Brown, 2003: Mountaintop and radar measurements of anthropogenic aerosol effects on snow growth and snowfall rate. *Geophys. Res. Lett.*, **30**, 1538, <https://doi.org/10.1029/2002GL016855>.
- Chen, J.-P., 1994: Theory of deliquescence and modified Kohler curves. *J. Atmos. Sci.*, **51**, 3505–3516, [https://doi.org/10.1175/1520-0469\(1994\)051<3505:TODAMK>2.0.CO;2](https://doi.org/10.1175/1520-0469(1994)051<3505:TODAMK>2.0.CO;2).
- , and D. Lamb, 1994: The theoretical basis for the parameterization of ice crystal habits: Growth by vapor deposition. *J. Atmos. Sci.*, **51**, 1206–1222, [https://doi.org/10.1175/1520-0469\(1994\)051<1206:TTBFTP>2.0.CO;2](https://doi.org/10.1175/1520-0469(1994)051<1206:TTBFTP>2.0.CO;2).
- , and T.-C. Tsai, 2016: Triple-moment modal parameterization for the adaptive growth habit of pristine ice crystals. *J. Atmos. Sci.*, **73**, 2105–2122, <https://doi.org/10.1175/JAS-D-15-0220.1>.
- , A. Hazra, and Z. Levin, 2008: Parameterizing ice nucleation rates using contact angle and activation energy derived from laboratory data. *Atmos. Chem. Phys.*, **8**, 7431–7449, <https://doi.org/10.5194/acp-8-7431-2008>.
- de Boer, G., T. Hashino, and G. J. Tripoli, 2010: Ice nucleation through immersion freezing in mixed-phase stratiform clouds: Theory and numerical simulations. *Atmos. Res.*, **96**, 315–324, <https://doi.org/10.1016/j.atmosres.2009.09.012>.
- , H. Morrison, M. D. Shupe, and R. Hildner, 2011: Evidence of liquid dependent ice nucleation in high-latitude stratiform clouds from surface remote sensors. *Geophys. Res. Lett.*, **38**, L01803, <https://doi.org/10.1029/2010GL046016>.
- , T. Hashino, G. J. Tripoli, and E. W. Eloranta, 2013: A numerical study of aerosol influence on mixed-phase stratiform clouds through modulation of the liquid phase. *Atmos. Chem. Phys.*, **13**, 1733–1749, <https://doi.org/10.5194/acp-13-1733-2013>.
- DeMott, P. J., and Coauthors, 2010: Predicting global atmospheric ice nuclei distributions and their impacts on climate. *Proc. Natl. Acad. Sci. USA*, **107**, 11 217–11 222, <https://doi.org/10.1073/pnas.0910818107>.
- Diehl, K., and S. Wurzler, 2004: Heterogeneous drop freezing in the immersion mode: Model calculations considering soluble and insoluble particles in the drops. *J. Atmos. Sci.*, **61**, 2063–2072, [https://doi.org/10.1175/1520-0469\(2004\)061<2063:HDFITI>2.0.CO;2](https://doi.org/10.1175/1520-0469(2004)061<2063:HDFITI>2.0.CO;2).
- Dinh, T., and D. R. Durran, 2012: A hybrid bin scheme to solve the condensation/evaporation equation using a cubic distribution function. *Atmos. Chem. Phys.*, **12**, 1003–1011, <https://doi.org/10.5194/acp-12-1003-2012>.

- Findeisen, W., 1938: Kolloid-meteorologische Vorgänge bei Neiderschlags-bildung. *Meteor. Z.*, **55**, 121–133.
- Fridlind, A. M., A. S. Ackerman, G. McFarquhar, G. Zhang, M. R. Poellot, P. J. Demott, A. J. Prenni, and A. J. Heymsfield, 2007: Ice properties of single-layer stratocumulus during the mixed-phase Arctic cloud experiment: 2. Model results. *J. Geophys. Res.*, **112**, D24202, <https://doi.org/10.1029/2007JD008646>.
- , B. van Dierenhoven, A. S. Ackerman, A. Avramov, A. Mrowiec, H. Morrison, P. Zuidema, and M. D. Shupe, 2012: A FIRE-ACE/SHEBA case study of mixed-phase Arctic boundary layer clouds: Entrainment rate limitations on rapid primary ice nucleation processes. *J. Atmos. Sci.*, **69**, 365–389, <https://doi.org/10.1175/JAS-D-11-052.1>.
- Gonda, T., and T. Yamazaki, 1984: Initial growth forms of snow crystals growing from frozen droplets. *J. Meteor. Soc. Japan*, **62**, 190–192, https://doi.org/10.2151/jmsj1965.62.1_190.
- Hansen, J., and Coauthors, 2005: Efficacy of climate forcings. *J. Geophys. Res.*, **110**, D18104, <https://doi.org/10.1029/2005JD005776>.
- Harrington, J. Y., D. Lamb, and R. Carver, 2009: Parameterization of surface kinetic effects for bulk microphysical models: Influences on simulated cirrus dynamics and structure. *J. Geophys. Res.*, **114**, D06212, <https://doi.org/10.1029/2008JD011050>.
- , K. Sulia, and H. Morrison, 2013: A method for adaptive habit prediction in bulk microphysical models. Part I: Theoretical development. *J. Atmos. Sci.*, **70**, 349–364, <https://doi.org/10.1175/JAS-D-12-040.1>.
- Hashino, T., and G. J. Tripoli, 2007: The Spectral Ice Habit Prediction System (SHIPS). Part I: Model description and simulation of vapor deposition process. *J. Atmos. Sci.*, **64**, 2210–2237, <https://doi.org/10.1175/JAS3963.1>.
- , and —, 2008: The Spectral Ice Habit Prediction System (SHIPS). Part II: Simulation of nucleation and depositional growth of polycrystals. *J. Atmos. Sci.*, **65**, 3071–3094, <https://doi.org/10.1175/2008JAS2615.1>.
- , and G. Tripoli, 2011a: The Spectral Ice Habit Prediction System (SHIPS). Part III: Description of the ice particle model and the habit-dependent aggregation model. *J. Atmos. Sci.*, **68**, 1125–1141, <https://doi.org/10.1175/2011JAS3666.1>.
- , and —, 2011b: The Spectral Ice Habit Prediction System (SHIPS). Part IV: Box model simulations of habit-dependent aggregation process. *J. Atmos. Sci.*, **68**, 1142–1161, <https://doi.org/10.1175/2011JAS3667.1>.
- , M. Satoh, Y. Hagihara, T. Kubota, T. Matsui, H. Okamoto, and T. Nasuno, 2013: Evaluating cloud microphysics from NICAM against CloudSat and CALIPSO. *J. Geophys. Res. Atmos.*, **118**, 7273–7292, <https://doi.org/10.1002/jgrd.50564>.
- , and Coauthors, 2016: Evaluating Arctic cloud radiative effects simulated by NICAM with A-train. *J. Geophys. Res. Atmos.*, **121**, 7041–7063, <https://doi.org/10.1002/2016JD024775>.
- Hoose, C., and O. Mohler, 2012: Heterogeneous ice nucleation on atmospheric aerosols: A review of results from laboratory experiments. *Atmos. Chem. Phys.*, **12**, 9817–9854, <https://doi.org/10.5194/acp-12-9817-2012>.
- Iacono, M. J., J. S. Delamere, E. J. Mlawer, M. W. Shephard, S. A. Clough, and W. D. Collins, 2008: Radiative forcing by long-lived greenhouse gases: Calculations with the AER radiative transfer models. *J. Geophys. Res.*, **113**, D13103, <https://doi.org/10.1029/2008JD009944>.
- Ishimoto, H., 2008: Radar backscattering computations for fractal-shaped snowflakes. *J. Meteor. Soc. Japan*, **86**, 459–469, <https://doi.org/10.2151/jmsj.86.459>.
- Jensen, A. A., J. Y. Harrington, H. Morrison, and J. A. Milbrandt, 2017: Predicting ice shape evolution in a bulk microphysics model. *J. Atmos. Sci.*, **74**, 2081–2104, <https://doi.org/10.1175/JAS-D-16-0350.1>.
- Khvorostyanov, V. I., and J. A. Curry, 2014: *Thermodynamics, Kinetics, and Microphysics of Clouds*. Cambridge University Press, 782 pp.
- Korolev, A., G. A. Isaac, and J. Hallett, 2000: Ice particle habits in stratiform clouds. *Quart. J. Roy. Meteor. Soc.*, **126**, 2873–2902, <https://doi.org/10.1002/qj.49712656913>.
- , M. P. Bailey, J. Hallett, and G. A. Isaac, 2004: Laboratory and in situ observation of deposition growth of frozen drops. *J. Appl. Meteor.*, **43**, 612–622, [https://doi.org/10.1175/1520-0450\(2004\)043<0612:LAISOO>2.0.CO;2](https://doi.org/10.1175/1520-0450(2004)043<0612:LAISOO>2.0.CO;2).
- Lance, S., and Coauthors, 2011: Cloud condensation nuclei as a modulator of ice processes in Arctic mixed-phase clouds. *Atmos. Chem. Phys.*, **11**, 8003–8015, <https://doi.org/10.5194/acp-11-8003-2011>.
- Liu, G., 2008: A database of microwave single-scattering properties for nonspherical ice particles. *Bull. Amer. Meteor. Soc.*, **89**, 1563–1570, <https://doi.org/10.1175/2008BAMS2486.1>.
- Liu, H.-C., P. K. Wang, and R. E. Schlesinger, 2003: A numerical study of cirrus clouds. Part II: Effects of Ambient temperature, stability, radiation, ice microphysics, and microdynamics on cirrus evolution. *J. Atmos. Sci.*, **60**, 1097–1119, [https://doi.org/10.1175/1520-0469\(2003\)060<1097:ANSOCC>2.0.CO;2](https://doi.org/10.1175/1520-0469(2003)060<1097:ANSOCC>2.0.CO;2).
- Liu, X., and Coauthors, 2011: Testing cloud microphysics parameterizations in NCAR CAM5 with ISDAC and M-PACE observations. *J. Geophys. Res.*, **116**, D00T11, <https://doi.org/10.1029/2011JD015889>.
- Maahn, M., and U. Löhnert, 2017: Potential of higher-order moments and slopes of the radar Doppler spectrum for retrieving microphysical and kinematic properties of Arctic ice clouds. *J. Appl. Meteor. Climatol.*, **56**, 263–282, <https://doi.org/10.1175/JAMC-D-16-0020.1>.
- Manabe, S., and R. T. Wetherald, 1975: The effects of doubling the CO₂ concentration on the climate of a general circulation model. *J. Atmos. Sci.*, **32**, 3–15, [https://doi.org/10.1175/1520-0469\(1975\)032<0003:TEODTC>2.0.CO;2](https://doi.org/10.1175/1520-0469(1975)032<0003:TEODTC>2.0.CO;2).
- Matrosov, S. Y., C. G. Schmitt, M. Maahn, and G. de Boer, 2017: Atmospheric ice particle shape estimates from polarimetric radar measurements and in situ observations. *J. Atmos. Oceanic Technol.*, **34**, 2569–2587, <https://doi.org/10.1175/JTECH-D-17-0111.1>.
- Mitchell, D. L., A. Huggins, and V. Grubisic, 2006: A new snow growth model with application to radar precipitation estimates. *Atmos. Res.*, **82**, 2–18, <https://doi.org/10.1016/j.atmosres.2005.12.004>.
- Morrison, H., and Coauthors, 2011: Intercomparison of cloud model simulations of Arctic mixed-phase boundary layer clouds observed during SHEBA/FIRE-ACE. *J. Adv. Model. Earth Syst.*, **3**, M06003, <https://doi.org/10.1029/2011MS000066>.
- , G. de Boer, G. Feingold, J. Harrington, M. D. Shupe, and K. Sulia, 2012: Resilience of persistent Arctic mixed-phase clouds. *Nat. Geosci.*, **5**, 11–17, <https://doi.org/10.1038/ngeo1332>.
- Nishizawa, T., H. Okamoto, T. Takemura, N. Sugimoto, I. Matsui, and A. Shimizu, 2008: Aerosol retrieval from two-wavelength backscatter and one-wavelength polarization lidar measurement taken during the MR01K02 cruise of the R/V Mirai and evaluation of a global aerosol transport model. *J. Geophys. Res.*, **113**, D21201, <https://doi.org/10.1029/2007JD009640>.
- Okamoto, H., 2002: Information content of the 95-GHz cloud radar signals: Theoretical assessment of effects of nonsphericity and

- error evaluation of the discrete dipole approximation. *J. Geophys. Res.*, **107**, 4628, <https://doi.org/10.1029/2001JD001386>.
- , S. Iwasaki, M. Yasui, H. Horie, H. Kuroiwa, and H. Kumagai, 2003: An algorithm for retrieval of cloud microphysics using 95-GHz cloud radar and lidar. *J. Geophys. Res.*, **108**, 4226, <https://doi.org/10.1029/2001JD001225>.
- , and Coauthors, 2007: Vertical cloud structure observed from shipborne radar and lidar: Midlatitude case study during the MR01/K02 cruise of the Research Vessel Mirai. *J. Geophys. Res.*, **112**, D08216, <https://doi.org/10.1029/2006JD007628>.
- , and Coauthors, 2008: Vertical cloud properties in the tropical western Pacific Ocean: Validation of the CCSR/NIES/FRCGC GCM by shipborne radar and lidar. *J. Geophys. Res.*, **113**, D24213, <https://doi.org/10.1029/2008JD009812>.
- Paukert, M., and C. Hoose, 2014: Modeling immersion freezing with aerosol-dependent prognostic ice nuclei in Arctic mixed-phase clouds. *J. Geophys. Res. Atmos.*, **119**, 9073–9092, <https://doi.org/10.1002/2014JD021917>.
- Pinsky, M., A. Khain, and A. Korolev, 2015: Phase transformations in an ascending adiabatic mixed-phase cloud volume. *J. Geophys. Res. Atmos.*, **120**, 3329–3353, <https://doi.org/10.1002/2015JD023094>.
- Pruppacher, H. R., and J. D. Klett, 1997: *Microphysics of Clouds and Precipitation*. Kluwer Academic, 954 pp.
- Rangno, A. L., and P. V. Hobbs, 2001: Ice particles in stratiform clouds in the Arctic and possible mechanisms for the production of high ice concentrations. *J. Geophys. Res.*, **106**, 15 065–15 075, <https://doi.org/10.1029/2000JD900286>.
- Savre, J., and A. M. L. Ekman, 2015: A theory-based parameterization for heterogeneous ice nucleation and implications for the simulation of ice processes in atmospheric models. *J. Geophys. Res. Atmos.*, **120**, 4937–4961, <https://doi.org/10.1002/2014JD023000>.
- Serreze, M. C., A. P. Barrett, J. C. Stroeve, D. N. Kindig, and M. M. Holland, 2009: The emergence of surface-based Arctic amplification. *Cryosphere*, **3**, 11–19, <https://doi.org/10.5194/tc-3-11-2009>.
- Shupe, M., and J. M. Intrieri, 2004: Cloud radiative forcing of the Arctic surface: The influence of cloud properties, surface albedo, and solar zenith angle. *J. Climate*, **17**, 616–628, [https://doi.org/10.1175/1520-0442\(2004\)017<0616:CRFOTA>2.0.CO;2](https://doi.org/10.1175/1520-0442(2004)017<0616:CRFOTA>2.0.CO;2).
- , T. Uttal, S. Matrosov, and A. Frisch, 2001: Cloud water contents and hydrometeor sizes during the FIRE Arctic Clouds Experiment. *J. Geophys. Res.*, **106**, 15 015–15 028, <https://doi.org/10.1029/2000JD900476>.
- Sulia, K. J., and J. Y. Harrington, 2011: Ice aspect ratio influences on mixed-phase clouds: Impacts on phase partitioning in parcel models. *J. Geophys. Res.*, **116**, D21309, <https://doi.org/10.1029/2011JD016298>.
- Tripoli, G. J., and E. A. Smith, 2014a: Introducing variable-step topography (VST) coordinates within dynamically constrained nonhydrostatic modeling system (NMS). Part 1: VST formulation within NMS host model framework. *Dyn. Atmos. Oceans*, **66**, 28–57, <https://doi.org/10.1016/j.dynatmoce.2014.01.001>.
- , and —, 2014b: Introducing variable-step topography (VST) coordinates within dynamically constrained nonhydrostatic modeling system (NMS). Part 2: VST performance on orthodox obstacle flows. *Dyn. Atmos. Oceans*, **66**, 10–27, <https://doi.org/10.1016/j.dynatmoce.2014.01.003>.
- Uttal, T., and Coauthors, 2002: Surface heat budget of the Arctic Ocean. *Bull. Amer. Meteor. Soc.*, **83**, 255–276, [https://doi.org/10.1175/1520-0477\(2002\)083<0255:SHBOTA>2.3.CO;2](https://doi.org/10.1175/1520-0477(2002)083<0255:SHBOTA>2.3.CO;2).
- Walko, R., W. Cotton, G. Feingold, and B. Stevens, 2000: Efficient computation of vapor and heat diffusion between hydrometeors in a numerical model. *Atmos. Res.*, **53**, 171–183, [https://doi.org/10.1016/S0169-8095\(99\)00044-7](https://doi.org/10.1016/S0169-8095(99)00044-7).
- Wegener, A., 1911: *Thermodynamik der Atmosphäre*. J. A. Barth, 331 pp.
- Wen, G., M. Oue, A. Protat, J. Verlinde, and H. Xiao, 2016: Ice particle type identification for shallow arctic mixed-phase clouds using X-band polarimetric radar. *Atmos. Res.*, **182**, 114–131, <https://doi.org/10.1016/j.atmosres.2016.07.015>.
- Yoshimori, M., A. Abe-Ouchi, and A. Laine, 2017: The role of atmospheric heat transport and regional feedbacks in the Arctic warming at equilibrium. *Climate Dyn.*, **49**, 3457–3472, <https://doi.org/10.1007/s00382-017-3523-2>.
- Young, G. Y., P. J. Connolly, H. M. Jones, and T. W. Choularton, 2017: Microphysical sensitivity of coupled springtime Arctic stratocumulus to modelled primary ice over the ice pack, marginal ice, and ocean. *Atmos. Chem. Phys.*, **17**, 4209–4227, <https://doi.org/10.5194/acp-17-4209-2017>.